

https://dspace.org/

# Study of the underlying event and color reconnection in tt events at s = 13 Tev

**Rafanoharana, Dimbiniaina Soanasolo**

**2019**
https://hdl.handle.net/10539/28081

Downloaded from a DSpace repository. https://dspace.org/

# Study of the underlying event and color reconnection in $t\bar{t}$ events at $\sqrt{s} = 13$ TeV

*Author:*
**Dimbiniaina Soanasolo Rafanoharana**

*Supervisor:*
**Dr. Deepak Kar**

*Submitted in fulfillment of the requirements for the degree of Master of Science*




Faculty of Science
School of Physics

June 11, 2019

# Abstract


**Study of the underlying event and color reconnection in $t\bar{t}$ events at $\sqrt{s} = 13$ TeV**

by Dimbiniaina Soanasolo Rafanoharana

For the first part of this work, we introduce an improvement to the transverse plane method to reduce the effect of the hard interactions on the toward or the trans-min region, which in principle should increase the sensitivity of these regions to the underlying event. We perform a particle level study to identify class of events — based on the values of the event shape observables — for which these regions are less contaminated by jets from the hard interaction. We applied this method on $Z$-boson events and on $t\bar{t}$ events in the dimuon decay channel. For the $Z$-boson events, we find that the toward region for spherical events is less sensitive to these jets. For the $t\bar{t}$ events, we also find that the trans-min region for spherical events is less sensitive to these jets. In addition, using the data collected by the ATLAS detector in 2015 and 2016, measurements of observables defined using this method are compared to the prediction of Monte Carlo event generators for the $t\bar{t}$ di-muon channel.

For the second part of this work, we study the sensitivity to color reconnection of observables defined using the spread of charged particles between a pair of jets. We expect that the color field spanned between a pair of color connected partons, would enhance the production of particles between them. Using the $t\bar{t}$ all hadronic decay channel, with boosted top quarks, we perform a particle level study to test if there is a difference between the distribution of these observables for a pair of color connected and a pair of non color connected jets.

# Declaration

I, Dimbiniaina Soanasolo Rafanoharana, declare that this dissertation titled, "Study of the underlying event and color reconnection in $t\bar{t}$ events at $\sqrt{s} = 13$ TeV" is my own work. It has not been submitted before for any degree or examination at any other University.

Signed: 

Date: June 11, 2019

# Acknowledgments

My sincere gratitude goes to my supervisor Dr. Deepak Kar, for his guidance, advice and for teaching me the necessary skills for this work.

This work would not have been possible without the financial support from the African Institute for Mathematical Sciences (AIMS) and the National Research Foundation (NRF). I am also grateful to Wits HEP group and the SA-CERN consortium for their support allowing me to attend workshops and conference.

I would like also to thank Dr. Debarati Roy and Shayma' Wahdan for their help on using ATLAS software.

My special thanks to all of my friends for everything.

Special acknowledgments to my family Dada sy Neny, Hariniaina sy Zarasoa for their unconditional support and encouragement.

# Research Outputs

## Published Paper:

D. Kar and D.S. Rafanoharana, *Probing underlying event in Z-boson events using event shape observables*, Int. J. Mod. Phys. A, Vol. 34.

## Conference and Workshop Outputs

Oral Presentation: 'Probing underlying event using event shape observables in Z-boson events' at the High Energy Particle Physics workshop (HEPP 2018), Stellenbosch Institute for Advanced Study, February 2018.

Oral Presentation: 'Probing underlying event using event shape observables in $t\bar{t}$ events at $\sqrt{s} = 13$ TeV' at the Annual Conference of the South African Institute of Physics (SAIP), Free State University, June 2018.

Oral Presentation: 'Probing color reconnection in $t\bar{t}$ events at $\sqrt{s} = 13$ TeV' at the High Energy Particle Physics workshop (HEPP 2019), Nelson Mandela University, February 2019.

# Contents

**Abstract** ii

**Declaration** iii

**Acknowledgments** iv

**Research Outputs** v

**1 Introduction** 1

**2 Theoretical Background** 3

2.1 The Standard Model of Particle Physics . . . . . 3

2.1.1 Fermions . . . . . 4

2.1.2 Fundamental Interactions and Bosons . . . . . 6

2.2 Phenomenology of proton-proton collision . . . . . 9

**3 The ATLAS detector at the LHC** 12

3.1 Overview of the Large Hadron Collider at CERN . . . . . 12

3.2 ATLAS experiment . . . . . 13

3.2.1 ATLAS coordinate system . . . . . 13

3.2.2 ATLAS subdetectors system . . . . . 14

**4 Measurement of observables sensitive to the underlying event** 16

4.1 Study of observables sensitive to the underlying event using the event shape observables in a Drell-Yan process producing a $Z$-boson events at $\sqrt{s} = 13$ TeV . . . . . 19

4.1.1 Event simulation and selection . . . . . 20

4.1.2 Definition of the observables . . . . . 21
4.1.3 Analysis and results . . . . . 22
4.1.4 Conclusion . . . . . 27
4.2 Measurement of observables sensitive to the underlying event in $t\bar{t}$ events at $\sqrt{s} = 13$ TeV . . . . . 28
4.2.1 Data and MC simulation samples . . . . . 29
4.2.2 Object reconstruction and identification . . . . . 30
4.2.3 Event selection . . . . . 33
4.2.4 Methodology . . . . . 33
4.2.5 Results . . . . . 37

**5 Study of the color reconnection in all hadronic $t\bar{t}$ events 44**
5.1 Aim . . . . . 45
5.2 Methodology . . . . . 46
5.3 Event simulation and selection . . . . . 48
5.4 Methodology and results . . . . . 48
5.4.1 For a large radius jet with three subjets . . . . . 49
5.4.2 For a large radius jet with four subjets . . . . . 51

**6 Conclusions 56**

**Bibliography 57**

# List of Tables

2.1 The four fundamental forces with their relative strength to gravity, their range and their associated charge. . . . . 4

# List of Figures


2.1 Elementary particles described in the Standard Model . . . . . 5

2.2 Feynman diagram of the QED interaction vertex. . . . . 6

2.3 Feynman diagram of the QCD interaction vertices. . . . . 7

2.4 Feynman diagram of the weak interaction vertices. . . . . 8

2.5 Sketch of a proton-proton collision as simulated by an event generator. 11

3.1 The accelerator complex at CERN. . . . . 13

3.2 Illustration of the ATLAS coordinate system. . . . . 14

3.3 The ATLAS detector. . . . . 15

4.1 Definition of the UE regions as a function of the azimuthal angle with respect to the leading direction . . . . . 17

4.2 Feynman diagram of a Drell-Yan process producing a $Z$-boson decaying into muon pairs. . . . . 19

4.3 Distribution of the thrust $T$ and the sphericity $S$. . . . . 23

4.4 The mean of the sum of the transverse momentum density, and the mean of the multiplicity density of charged particles in the toward region as a function of the momentum the $Z$-boson $Z_{p_T}$ . . . . . 24

4.5 The mean of the sum of the transverse momentum density and the mean of the multiplicity density of charged particles in the toward region as a function of the thrust $T$ for $Z$-boson events. . . . . 26

4.6 The mean of the sum of the transverse momentum density and the mean of the multiplicity density of charged particles in the toward region as a function of the sphericity $S$ for $Z$-boson events. . . . . 27

4.7 The mean of the sum of the transverse momentum density, and the mean of the multiplicity density of charged particles in the trans-min region as a function of the sphericity for $t\bar{t}$ events. . . . . 36
4.8 The mean of the sum of the transverse momentum density, and the mean of the multiplicity density of charged particles in the trans-min region as a function of the thrust $T$ for $t\bar{t}$ events. . . . . 36
4.9 The mean of the sum of the transverse momentum density, the mean of the multiplicity density, and the mean of the mean transverse momentum of charged particles in the trans-min, trans-max and transverse region as a function of the $p_T^{t\bar{t}}$. . . . . 39
4.10 The mean of the sum of the transverse momentum density, the mean of the multiplicity density, and the mean of the mean transverse momentum of charged particles in the trans-min region for $S > 0.75$ and for $S \leq 0.75$ as a function of the $p_T^{t\bar{t}}$. . . . . 40
4.11 The mean of the sum of the transverse momentum density, the mean of the multiplicity density, and the mean of the mean transverse momentum of charged particles in the trans-min for $T < 0.7$ and for $T \geq 0.7$ as a function of the $p_T^{t\bar{t}}$. . . . . 41
4.12 Distribution of the sum of the transverse momentum density of charged particles, and the charged particles multiplicity density for events with $S \leq 0.75$. . . . . 42
4.13 Distribution of the sum of the transverse momentum density of charged particles, and the charged particles multiplicity density for events with $S > 0.75$. . . . . 42
4.14 Distribution of the sum of the transverse momentum density of charged particles, and the charged particles multiplicity density for events with $T \geq 0.7$. . . . . 43
4.15 Distribution of the sum of the transverse momentum density of charged particles, and the charged particles multiplicity density for events with $T < 0.7$. . . . . 43

5.1 Illustration of a string breaking by quark pair creation in the string field, and the motion and breakup of a string system. . . . . 44

5.2 QCD color propagation rules for elementary quark-gluon and triple gluon vertex. . . . . 45
5.3 Feynman diagram with the QCD color propagation rule for a $t\bar{t}$ all hadronic channel. . . . . 46
5.4 A representation of a large radius jet with its subjets in the $\eta - \phi$ plane. 47
5.5 Diagram illustrating the rectangular region between jets. . . . . 48
5.6 Feynman diagrams with the color propagation rule of a $t$-quark decaying with and without additionnal radiative gluon from the $b$-quark. . . . . 49
5.7 Distribution of the number of subjets inside large radius jet . . . . . 50
5.8 Examples of subjets configuration inside large radius jet. . . . . 50
5.9 Distributions of the sum of the transverse momentum density and multiplicity density of charged particles for large radius jet with three subjets. 54
5.10 Distributions of the sum of the transverse momentum density and multiplicity density of charged particles for large radius jet with four subjets. 55

# Chapter 1

# Introduction

In hadronic collisions like at the Large Hadron Collider (LHC), the actual interactions occur between the partons inside the two hadrons rather than between the two hadrons themselves. Thus different partonic interactions can occur in the same hadron-hadron collision. The *hard scatter process* (HS), which is the short-distance interaction between two partons, is the process of real interest in the collision. In addition, there are the accompanying interactions collectively termed *underlying event* (UE), which consists of the *multiple parton interactions* (MPI) — the additional semi-hard partonic interactions —, and the *beam-beam remnants* (BBR) – the remaining partons inside the protons not interacting during the collision [1]. Furthermore, additional interactions and interferences can occur between these partons. In fact, as a result of color confinement, gluon fields, that are formed between these colored particles, can overlap and interact among them. *Color reconnection* (CR) is the mechanism that describes the dynamics and interactions of these chromoelectric fields [1].

However, the description of UE and CR are not known from first principle. In fact, both involve soft interactions that perturabative Quantum Chromodynamics (pQCD) can not be used. As a result, they are generally described using QCD inspired model with free parameters that need to be tuned. Yet, particles produced from these interactions cannot be experimentally identifiable, thus the main challenge when constraining the modeling of UE and CR is to define observables that have strong sensitivity to them .

The modeling of these two soft-QCD interactions are currently one of the main sources of uncertainty in precise measurement of the properties of the top quark.

Measurements of observables sensitive to the UE and CR are then critical in order to constrain the modeling of these soft-QCD interactions. The aim of the present work is to define observables that have strong sensitivity to the UE (CR mechanism), so that measurements of these observables can be used to tune the free parameters of the different UE (CR) models.

This work is organized as follows. Chapter 2 reviews important theoretical background relevant for this work. Study of the underlying event in $Z$-boson and in $t\bar{t}$ events are presented in Chapter 3. Study of the CR mechanism is presented in Chapter 4.

# Chapter 2

# Theoretical Background

The theoretical framework relevant for this work is presented in this chapter. First, a brief introduction to the Standard Model of particle physics is given, where properties of elementary particles and their interactions are described. Then a summary of the phenomenology of hadron collision is presented.

## 2.1 The Standard Model of Particle Physics

Four fundamental interactions are currently known to exist in nature: the *electromagnetic*, the *weak*, the *strong* and the *gravitational force*. An overview of their properties are shown in Table 2.1. The weak and the strong force have both a very short range of action, which is below the order of femtometer ($10^{-15}$ m). They are only effective at the subatomic scale. The former acts on particles carrying a non-zero *weak isospin*, $I$ — which is the conserved charge of the $SU(2)_L$—, and the latter acts on particles with *color charge*, $C$. Electromagnetism is the force responsible for the interaction between objects with non-vanishing *electric charge* $Q$, whereas gravity is the force that occurs between objects with *mass* or *energy*. They have both an infinite range of action, thus they can affect the description of any physical object at any scale. Everyday phenomena are the result of the symbiosis between these two forces. However, on the one hand gravity by its own describes the physics of large scales, on the other hand it is too weaker compared to the other forces at the subatomic level.

*The Standard Model of Particle Physics* (SM) [2, 3, 4] is currently the most successful theory that the human kind has built to describe the dynamics and interactions of

| Interaction | Relative strength | Range (m) | Associated charge |
|---|---|---|---|
| Strong | $10^{38}$ | $10^{-15}$ | color charge $C$ |
| Weak | $10^{25}$ | $10^{-18}$ | weak isospin $I$ |
| Electromagnetic | $10^{36}$ | $\infty$ | electric charge $Q$ |
| Gravity | 1 | $\infty$ | mass or energy |

Table 2.1: The four fundamental forces with their relative strength to gravity, their range and their associated charge.

the currently known elementary particles in the Universe. It unifies in one framework three fundamental interactions — the electromagnetism, the weak and the strong force — that rules the subatomic world. It is a *renormalizable quantum field theory* (QFT) with a symmetry group

$$SU(3)_C \otimes SU(2)_L \otimes U(1)_Y, \tag{2.1}$$

where $SU(3)_C$ and $SU(2)_L \otimes U(1)_Y$ are respectively the symmetry group of the strong and the electroweak interaction. The charge associated to $SU(3)_C$ is the color charge $C$, which are the *red*, *blue*, and *green*. The charges associated to $SU(2)_L \otimes U(1)_Y$ are the weak isospin, $I$ and the hypercharge, $Y$.

In the SM, elementary particles can be categorized into *fermions* and *bosons*. Fermions — which have an *half-integer* spin — are particles that follow the Fermi-Dirac statistics. Visible matter are made of fermions. Bosons — which have an *interger* spin — are particles that follow the Bose-Einstein statistics. In the QFT description of the elementary particles, the interactions between fermions are described by the exchange of a gauge boson. In addition, each particle described in SM has its corresponding *anti-particle* [1]. Particle and its anti-particle have the same mass and spin, but with opposite values for the additive physical charge.

### 2.1.1 Fermions

Fermions — which have an *half-integer* spin — are particles that follow the Fermi-Dirac statistics. There are currently 12 known elementary fermions, that are categorized into *leptons* and *quarks*.

Leptons ($l$), shown in green in Figure 2.1, can be categorized into charged and neutral leptons. Charged leptons can interact via electroweak interaction. They are

[1] Some particles are their own anti-particles if all their physical charge are null.

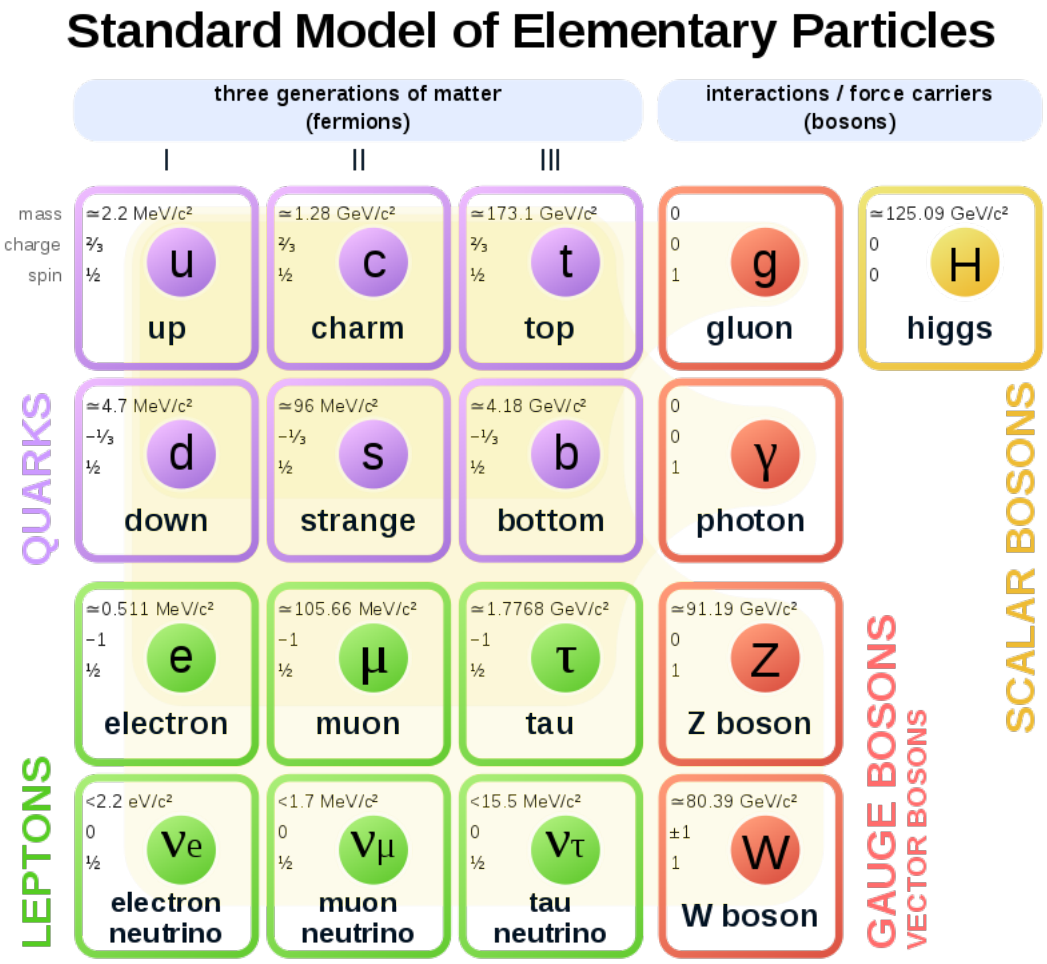



Figure 2.1: Elementary particles described in the Standard Model [21].

named *electron* $e^-$, *muon* ($\mu^-$), and *tau* ($\tau^-$) and they all carry one unit of the elementary charge $e$. Their anti-particles carry the same quantum numbers including the mass, but have a positive electric charge. Neutral leptons can only interact via weak interaction. They consist of the corresponding neutrino of each of these charged leptons. They are named *electron neutrino* $\nu_{e^-}$, *muon neutrino* $\nu_{\mu^-}$ and *tau neutrino* $\nu_{\tau^-}$. Their anti-particles are believed to be themselves.

Quarks ($q$), shown in purple in Figure 2.1, are the only fermions in the SM that carry color charge. They are grouped into *up-type* and *down-type* quark. The former consists of the *up* ($u$), *charm* ($c$) and *top* ($t$) quark. They all have an electric charge $Q = +2/3$. The latter includes the *down* ($d$), *strange* ($s$) and *bottom* ($b$) quark. They all have an electric charge $Q = -1/3$. The anti-quark ($\bar{q}$) has the same intrinsic properties as the quark, but has the opposite electric charge and instead carries an

*anti-color* charge: *anti-red* ($\bar{r}$), *anti-blue* ($\bar{b}$) and *anti-green* ($\bar{g}$). Quarks are the only particles that can interact via the four fundamental interactions in nature.

These fermions can be further categorized into generations or families based on their stability. The stability of particles in each generation decreases from lower to higher generation. The first 3 columns of Figure 2.1 represents the 3 generations of fermions. Each family consists of two quarks — one up-type quark and its down-type partner — and 2 leptons – one charged leptons and its neutrino partner. Stable particles that make ordinary matter, belong to the first generation of fermions.

### 2.1.2 Fundamental Interactions and Bosons

#### 2.1.2.1 Electromagnetic Interaction

The electromagnetic interaction is mathematically described by *Quantum Electrodynamics* (QED). It is an abelian field theory with the symmetry group $U(1)$. The electromagnetic interaction acts only on particles carrying non vanishing electric charge, and its force carrier is the massless and electrically neutral *photon*, $\gamma$. All electromagnetic interactions are built from the combination of the vertex photon-fermions-antifermions shown in Figure 2.2, where $f$ is an electrically charged fermion and $\bar{f}$ is its corresponding anti-particle.

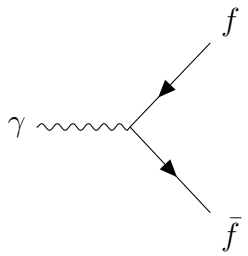



Figure 2.2: Feynman diagram of the QED interaction vertex.

#### 2.1.2.2 Strong interaction

The strong interaction is mathematically described by *Quantum Chromodynamics*. It only acts on particles carrying a non vanishing color charge. It is mediated by 8 massless and electrically neutral gluons, $g$. However, gluon itself carries one color charge and one anti-color charge, therefore gluon can couple to other gluons. All

strong interactions are built from the combination of the three basic vertex shown in Figure 2.3. There are two allowed self-gluon interactions, which are the triple and quartic vertices shown in Figure 2.3(b) and Figure 2.3(c), respectively. The third QCD vertex is the $q\bar{q}g$ vertex, shown in Figure 2.3(a), where the quark $q$ and anti-quark $\bar{q}$ have to be of the same flavor.

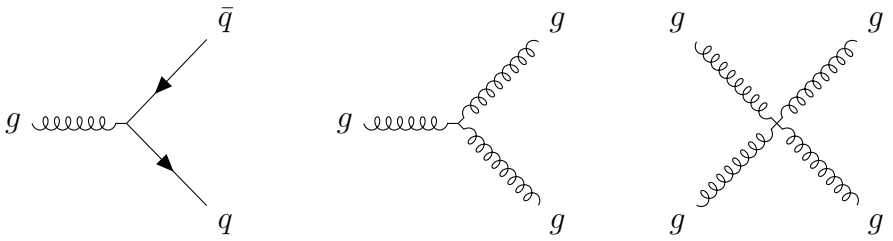



Figure 2.3: Feynman diagram of the QCD interaction vertices.

The strong interaction has two very important properties which are the *asymptotic freedom* and the *color confinement*. They are both a consequence of the property of the strong coupling constant, $\alpha_S$. In fact, the QCD coupling constant increases as the distance decreases, and decreases as the energy increases.

Thus at high energy or small distance, QCD becomes a weakly coupled interaction that quarks and gluons are considered free at this scale. Interactions at this energy scale, can be described using perturbative QCD as one can neglect terms in higher order of the strong coupling constant.

At low energy or large distance, the strong coupling constant diverges. Thus QCD becomes a strongly coupled interaction, that quarks and gluons are confided into a colorless hadron. Hadrons can be categorized into mesons and baryons. The former are made of two quarks carrying opposite color charge, and the latter are made of three quarks such that their net color charge is zero.

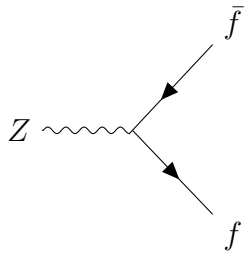
#### 2.1.2.3 Weak Interaction

The weak interaction is the only force that acts on all types of fermions. It has three massive boson mediators, which are the electrically neutral $Z$-boson, and the two charged $W^{\pm}$-bosons. There are two types of weak interactions depending on the boson mediators.

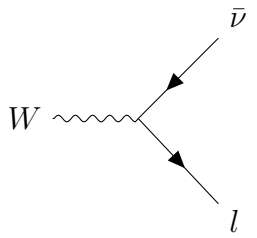
Neutral weak interaction is mediated by the electrically neutral $Z$-boson. The Feynman diagram that describes the neutral weak interaction is shown in Figure 2.4(a), where $f$ is a fermion and $\bar{f}$ is its corresponding anti-particle. Unlike QED, these fermions can be either electrically or neutral charged. Thus interactions mediated by a photon can also be mediated by a virtual $Z$-boson.

The charged weak interaction is mediated by the $W$-bosons. It is the only non-flavor-conserving SM interaction. In fact, its mediators can couple to fermions of different flavors as shown in Figure 2.4(b) and Figure 2.4(c). The former involves only leptons, where a $W$-boson couples to a charged lepton $l$ and its corresponding neutrino $\nu_l$. The latter involves only quarks, where a $W$-boson couples to a up-type quark $q_u$ and a down-type quark $q_d$.

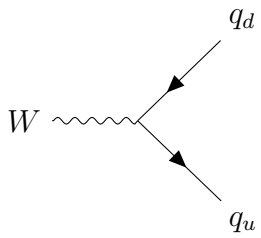
In addition, as $W$-bosons have a non-vanishing electric charge and weak isospin, thus self-interactions between the electroweak bosons are possible. Such interactions are shown in Figure 2.4(e) and Figure 2.4(d).



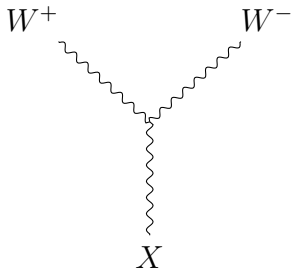

(a) Where $f$ is a fermion and $\bar{f}$ is its corresponding anti-particle.



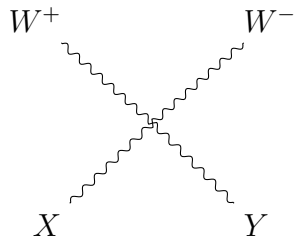

(b) Where $l$ is a charged lepton and $\nu$ is the corresponding neutrino.




(c) Where $q_u$ is an up-type quark and $q_d$ is an down-type quark.




(d) Where $X$ is a photon or a $Z$-boson.




(e) Where $X$ and $Y$ are any two electroweak bosons ($\gamma$, $Z$ or $W$) such that charge is conserved.

Figure 2.4: Feynman diagram of the weak interaction vertices.

#### 2.1.2.4 Higgs mechanism

The requirement of the electroweak interaction to be invariant under $SU(2)_L \otimes U(1)_Y$ is only possible if the electroweak gauge bosons are massless. However, experimental measurements show that the $Z$-boson and $W$-bosons are all massive particles. This issue was solved by the introduction of the *Higgs field*, where these electroweak bosons acquire their mass through their interaction with this new field [5, 6, 7, 8]. The existence of this field also implies the existence of one massive scalar boson named *Higgs bosons*. In 2012, ATLAS and CMS reported the observation of a new boson consistent with the Higgs boson [13, 14].

## 2.2 Phenomenology of proton-proton collision

Monte Carlo event generators are computer programs that provide detailed simulations of high-energy collisions [1]. The general idea of the simulation of hadronic collision by event generators are described in this section. More precisely, the simulation of an inelastic proton-proton collision is presented. A sketch of a typical proton-proton collision is shown in Figure 2.5.

In an inelastic proton-proton collision, the actual interactions occur between the partons inside the two protons rather than between the two protons themselves. The interacting partons can be the valence quarks of the proton and/or any partons from the sea of quarks and gluons inside the proton. Final state particles of a proton-proton collisions are the results of the evolution of these partons through different processes.

**Primary parton level interactions** Primary parton level interactions refer to the interactions between the partons constituents of the two colliding protons. These are:

- **The hard interaction subprocess** (HS) is the interaction between two partons with the highest momentum transfer during the proton-proton collision. It constitutes the process of real interest within the collision, as heavy resonance particles are produced through this mechanism. The coupling constant of this process is small ($\alpha_S << 1$), that the matrix element of the process can be computed using perturbative QCD at fixed order.

- **Initial and final state radiations** (I/FSR) are gluons and photons radiated by the initial and final state partons involved in the hard interaction subprocess. In fact, as a colored particles, these partons can always radiate QCD radiation as well as QED radiation.

- **The multiple parton interactions** (MPI) are the additional $2 \to 2$ semi-hard partonic processes to the hard-scattering process. In fact, at the energy scale that these protons collide, the partons inside them are asymptotically free. Thus one cannot prevent the possibility of having multiple $2 \to 2$ interactions in the same proton-proton collision. These interactions can be either hard or soft QCD interactions. Most current implementations of the modeling of these interactions are based on the perturbative model proposed by Sjöstrand and van Zijl [52]. These models have parameters that are not derived from first principle.

- **The beam remnant** is what is left out of the proton after the partons interacting through hard interaction and MPI are knocked out of the proton.

**Parton showering** Before reaching the hadronization scale $\Lambda_{QCD} \sim 1$ GeV, partons produced from these primary and secondary partonic interactions undergo a cascade of radiation, this phase of the evolution of the collision is referred to as parton shower. In fact, these partons can radiate gluons, while gluons themselves carry color charge, thus they can emit further gluon radiation. In MC event generators, parton shower algorithms which simulate this stage of the event, has parameters that can not be derived from theory.

**Hadronization process** The hadronization phase occurs when the momentum scale of the partons produced from the parton shower reach $\Lambda_{QCD} \sim 1$. It is the transition from the set of colored particles to the set of colorless hadrons. It is a non perturbative process. In the context of event generators, there are two main classes of hadronization models, which are the Lund string model [53] and the cluster model [54]. Hadrons produced after the hadronization process may decay further to produce the stable final state particles of a proton-proton collision.

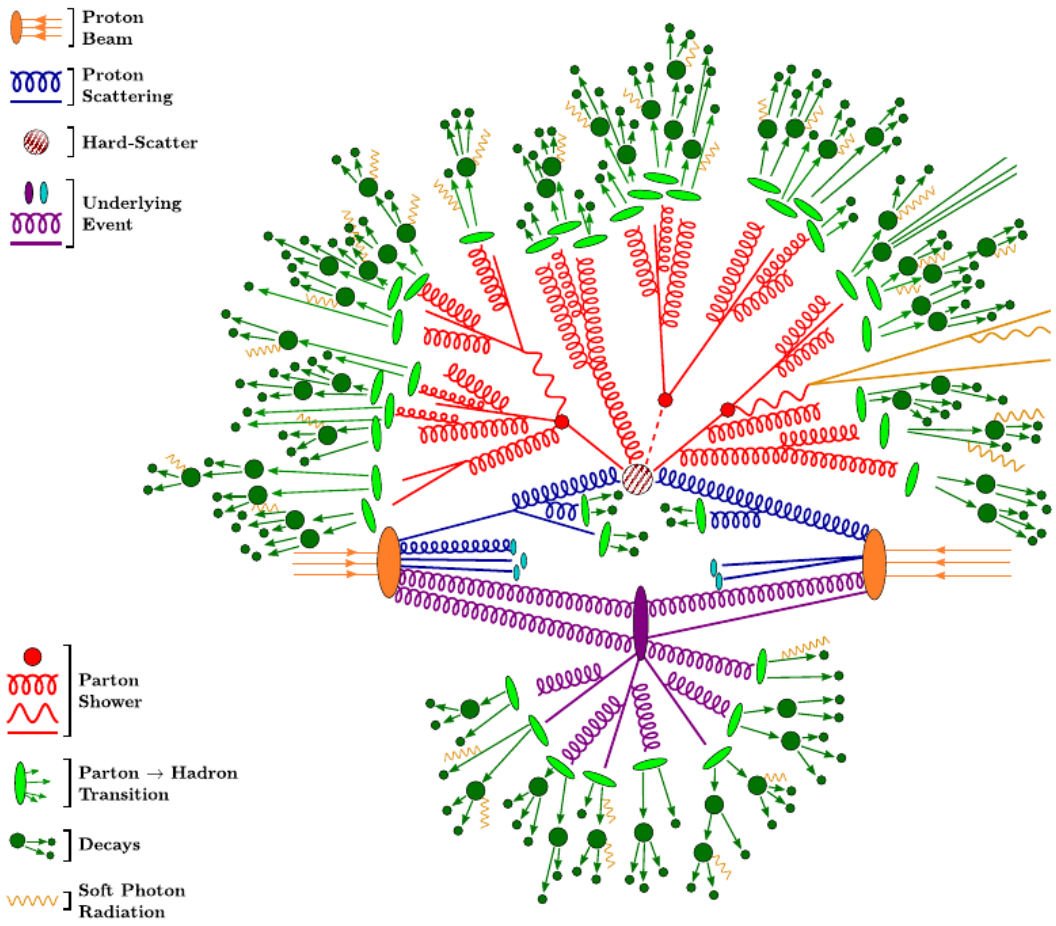



Figure 2.5: Sketch of a hadron-hadron collision as simulated by a Monte Carlo event generator. The red blob in the center represents the hard interaction, surrounded by a tree-like structure representing bremsstrahlung as simulated in parton showers. The purple blob represents a secondary hard multiple partons interaction. Hadronization process is represented by the light green blobs, dark green blobs indicate hadron decays, and yellow lines are soft photon radiation. [82]

**Color reconnection** Color reconnection (CR) is an ad-hoc mechanism in proton-proton collision. It occurs at any stages of an event where colored objects are present. Color reconnection is the mechanism that describes the dynamism and interactions of the gluon fields formed between two color connected particles i.e one quark or gluon of one color to quark or gluon with the corresponding anti-color. The CR mechanism can not be described from first principle and has to be modeled.

# Chapter 3

# The ATLAS detector at the LHC

## 3.1 Overview of the Large Hadron Collider at CERN

The *Large Hadron Collider* (LHC) [15] at the European Organization for Nuclear Research (CERN), is currently the largest particle accelerator in the world. It is located in the Swiss-French border. It is a circular accelerator with a circumference of 27 km. It is designed to produce a proton-proton, lead-lead or proton-lead collisions. For proton-proton collision, its designed centre-of-mass energy is 14 TeV with a maximum instantaneous luminosity of $10^{34}$ cm$^{-2}$ s$^{-1}$.

Before the two beams of protons are injected into the LHC ring, they are first accelerated through a multi-staged accelerator system. The beams of protons are first accelerated through the LINAC2 (Linear Accelerator). Once the beam energy reaches 50 MeV, they are injected into the Proton Synchrotron Booster that accelerates the beam up to 1.4 GeV. Then the beams pass successively through the Proton Synchrotron (PS) and the Super Proton Synchrotron (SPS) where they are accelerated to 25 GeV and 450 GeV, respectively.

The LHC is a synchrotron that accelerates two beams of protons or leads in opposite direction to collide them at four interaction points. At each of these points, there is a detector to record the properties of particles produced during the collision. These four detectors have different design depending on the physics purpose of the experiment. The LHCb (Large Hadron Collider beauty) [19] experiment focuses on the measurement of the CP violation in the interactions of $b$-hadrons in order to understand the asymmetry between matter and anti-matter in the Universe. The ALICE

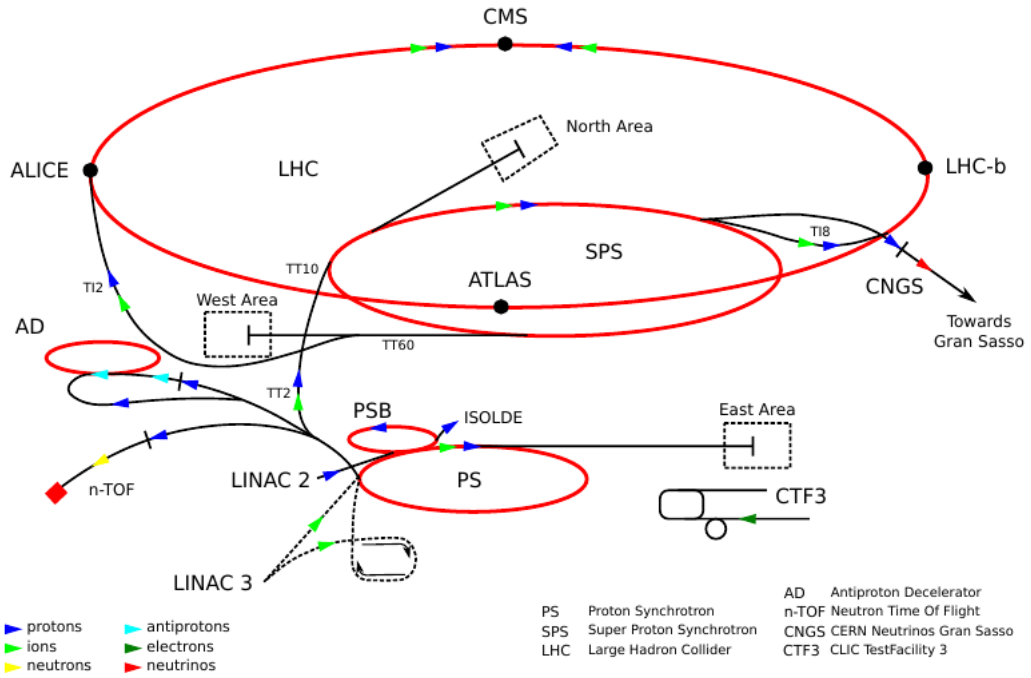



Figure 3.1: The accelerator complex at CERN. [21]

(A Large Ion Collider) [16] experiment focuses on the study of the quark-gluon plasma in order to understand color confinement. The CMS (Compact Muon Solenoid) [18], and ATLAS (A Toriodal LHC Apparatus) [17] experiments are both multi-purpose particle physics experiments. They are designed to perform precise SM measurements and to search for new physics.

## 3.2 ATLAS experiment

The ATLAS experiment is a multi-purpose particle physics experiments. The ATLAS detector is the largest particle collider detector. It has a 25 m of diameter, a 45 m in length, and a weight of 7,000 tons, that almost covers the $4\pi$ angle solid. An overview of the ATLAS detector is shown in Figure 3.3.

### 3.2.1 ATLAS coordinate system

The ATLAS experiment uses a right-handed coordinate system, as shown in Figure 3.2. The origin of the coordinates lies at the interaction point, the $x$-axis points toward the centre of LHC, the $y$-axis points upward, and the $z$-axis points along the beamline.

The azimuthal angle $\phi$ measures the angle in the $x-y$ plane with respect to the $x$-axis. The polar angle $\theta$ measures the angle in $z-y$ plane with respect to the $z$-axis.

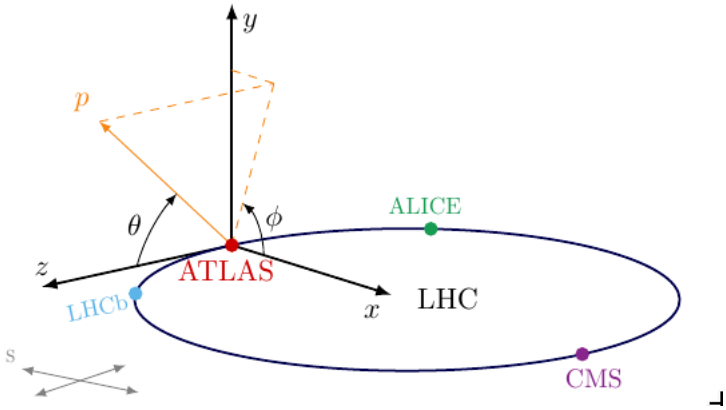



Figure 3.2: Illustration of the ATLAS coordinate system. [82]

Using these coordinates as well as the energy, $E$, and the Cartesian momentum of the particles, $\overrightarrow{p} = (p_x, p_y, p_z)$, we can define the following quantities which are more convenient to describe the properties of particles in collider physics:

- The rapidity, $y$, and the pseudorapidity, $\eta$, are defined respectively as

$$y := -ln\left[\frac{E+p_z}{E-p_z}\right] \quad \text{, and} \quad \eta := -ln\left[\tan\frac{\theta}{2}\right].$$

- The transverse energy, $E_T$, and the scalar transverse momentum, $p_T$, are defined respectively as

$$E_T := E\sin\theta \quad \text{, and} \quad p_T := \sqrt{p_x^2 + p_y^2}.$$

- The angular separation in the $\eta-\phi$ plane between two objects, $\Delta R$, is defined as

$$\Delta R := \sqrt{\Delta\phi + \Delta\eta}.$$

### 3.2.2 ATLAS subdetectors system

The ATLAS detector consists of multiple concentric detectors, that can mainly be grouped into three main subdetectors, which are the Inner Tracking Detector (ID), the Calorimeter Systems and the Muon Spectrometer (MS). An overview of the ATLAS detector is shown in Figure 3.3.

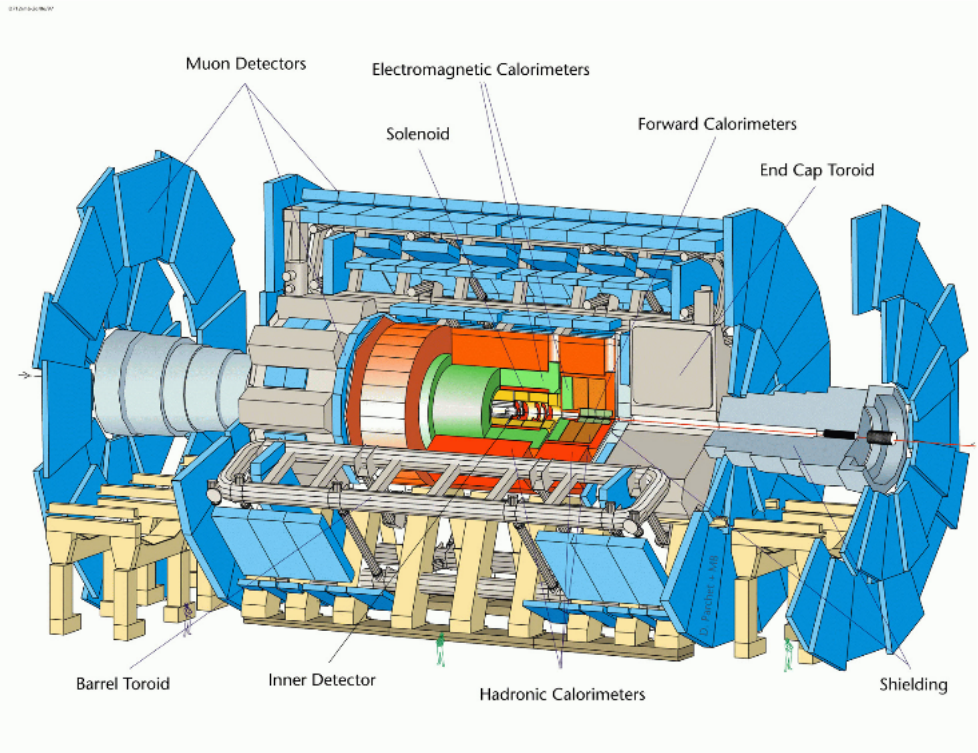



Figure 3.3: The ATLAS detector. [67]

**Inner Tracking Detector** The ID consists of Pixel Detector, Semiconductor Tracker (SCT), and Transition Radiation Tracker (TRT). It measures tracks deposited by charged particles when interacting with the detector material. It covers an angular region of $|\eta| < 2.5$, and can only measure momenta above 0.5 GeV.

**Calorimeter System** The Calorimeter System consists of the electromagnetic calorimeter (ECAL), and the hadronic calorimeter (HCAL). They are made of absorber material such that only muons and neutrinos (and any weakly interacting beyond SM particles) can traverse through it. The ECAL measures the energy of photons and electrons, and the HCAL measures the energy of hadrons.

**Muon Spectrometer** For normal operation, only muons are expected to reach the MS, as the SM particles should all be absorbed by the ECAL and the HCAL. The muon spectrometer measures the momenta of tracks up to 3 TeV and within $|\eta| < 2.7$.

# Chapter 4

# Measurement of observables sensitive to the underlying event

Soft-QCD parton level subprocesses in hadronic collision consist of the multiple parton interaction —the additional semi-hard partonic processes to the hard-scattering process — and the beam-beam remnants – the remaining partons inside the protons not interacting during the collision. Due to our inability to make predictions from first principle for any soft-QCD interactions, different models have been proposed to describe these hadronic subprocesses. Measurements of the properties of these soft interactions are critical to constrain the different models, and to tune their free parameters to perform precise Standard Model measurements or search for new physics phenomena at hadron colliders.

The underlying event is defined as the resultant of these soft-QCD primary subprocesses. However, only the properties of the final state particles produced by these partons can only be measured due color confinement. In addition, one cannot reconstruct observables purely using particles produced from these soft-QCD partons, as it is experimentally impossible to separate them from the final state particles initiated by the ISR and the FSR. Thus the main challenge when constraining the modeling of these soft interactions, is to construct observables that have a strong sensitivity to the MPI and the BBR, i.e observable with minimum contributions from the particles initiated by the ISR and FSR.

The *transverse plane method* was introduced by the CDF collaboration to define observables sensitive to the UE [34]. This method consists of dividing the transverse

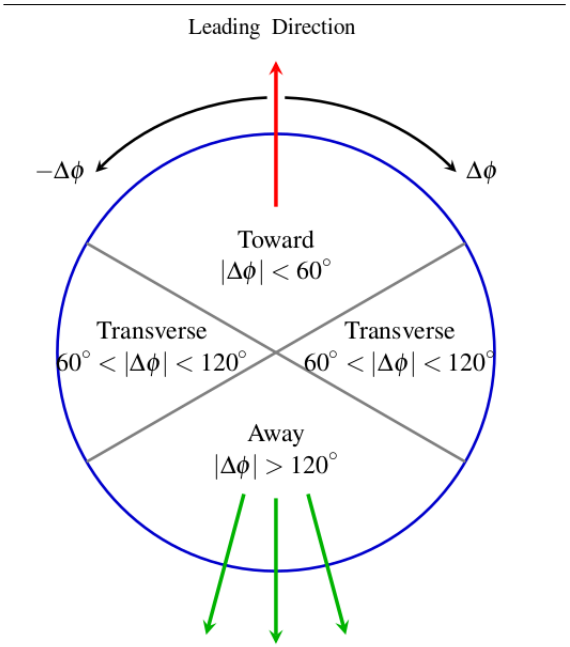



Figure 4.1: Definition of the UE regions as a function of the azimuthal angle with respect to the leading direction

.

plane to the two incoming protons into three regions based on their sensitivity to either the HS or the UE. The direction in which the HS particles mainly flow, is defined as the leading direction. Using the azimuthal angular difference with respect to the leading direction $|\Delta\phi| = |\phi - \phi_{Leading\ Direction}|$, one can define the following three azimuthal regions, as shown in Figure 4.1:

- The toward region, with $|\Delta\phi| < 60^o$, can be either sensitive to the UE or to the HS. For HS with colored objects in its final state, this region is likely to be contaminated by gluon radiation. While for a HS with a colorless object in its final state, QED bremsstrahlung might be produced in this regions, but that shouldn't not affect the sensitivity of the region to the UE.

- The transverse region, with $60^o < |\Delta\phi| < 120^o$, is sensitive to the UE as it is by construction perpendicular to the flow of the HS system.

- The away region, with $|\Delta\phi| > 120^o$, is sensitive to the HS. As it contains particles produced by the hadronization of partons balancing the momentum of partons interacting via HS.

This method has been the most prominently technique to define a UE sensitive

observables. However, limits of this method were seen in different measurements, which will be discussed in more details in section 4.1. In this work, we introduce an improvement to this transverse plane method using event shape observables to select events, for which the UE sensitive regions, defined using this usual method, are less contaminated by particles initiated by the ISR and FSR. In section 4.1, the sensitivity of these regions to the ISR and FSR is studied using that improved method in a Drell-Yan events producing $Z$-boson. In section 4.2, a preliminary results of measurement of the observables sensitive to the UE in the $t\bar{t}$ events is shown.

## 4.1 Study of observables sensitive to the underlying event using the event shape observables in a Drell-Yan process producing a $Z$-boson events at $\sqrt{s} = 13$ TeV

The Drell-Yan process producing a $Z$-boson decaying into lepton pairs, $Z \rightarrow l^+l^-$, presents a cleaner final state for measuring the UE activity in hadron collider. Due to the absence of colored objects in its final state, as shown in Figure 4.2, the only QCD hard objects susceptible of contaminating any defined observables sensitive to the UE are the jets initiated by gluons radiated by the initial state partons. For this reason, most of the measurements of observables sensitive to the UE by the CDF [22], ATLAS [26] and CMS experiments [29, 31] were performed in $Z$-boson events.

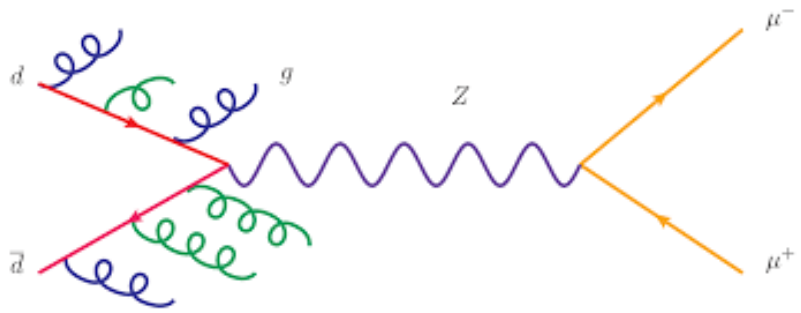



Figure 4.2: Feynman diagram of a Drell-Yan process producing a $Z$-boson decaying into muon pairs.

For a $Z$-boson event, the leading direction for the transverse plane method is considered as the transverse momentum of the $Z$-boson, which is by definition the sum of the transverse momentum of the lepton pairs. The sensitivity to either the hard subprocess or the UE of the three azimuthal regions in the transverse plane for a $Z$-boson event is as follow. The toward region, with $|\Delta\phi| < 60^o$, is sensitive to the UE as the $Z$-boson final state involve only colorless object. In addition to that, one can identify and exclude the contribution of two final state leptons. The transverse region, with $60^o < |\Delta\phi| < 120^o$, is sensitive to the UE as it is by construction perpendicular to the $Z$-boson system. The away region, with $|\Delta\phi| > 120^o$, is as usual sensitive to the hard process. It contains particles produced by the hadronization of partons balancing

the momentum of partons producing the $Z$-boson.

In the busy LHC environment, measurements of observables sensitive to the UE in $Z$-boson at $\sqrt{s} = 7$ TeV by the CMS [29] and ATLAS collaborations [26] show, that the toward region as well as the transverse region start receiving contribution from additional jets from the hard interaction process.

Measurements show differences in the sum of the transverse momentum density, $\sum p_T/\delta\eta\delta\phi$, and the multiplicity density, $N_{Chg}/\delta\eta\delta\phi$, of the charged particles between the two opposite transverse regions. That could only be explained by an asymmetrical production of additional jets in these two opposite regions. The region with more activity of charged particles is referred to as the *trans-max*, which should receive more contribution from the ISR. Whereas, the region with less activity of charged particles is referred to as the *trans-min* region, which should be less sensitive to the ISR.

The distribution of the sum of the transverse momentum density, $\sum p_T/\delta\eta\delta\phi$, in the toward region in $Z$-boson events also shows that this region start being contaminated by hard subprocess particles. In fact, measurement shows that the activity of charged particles in the toward region presents a dependency on the transverse momentum of the $Z$-boson $p_T^Z$. This would have been the same for all the $p_T^Z$ ranges, unless this region start receiving contributions from the additional jets initiated by hard scatter partons [26].

In this study, we introduce an additional approach to the usual transverse plane method for measuring observables sensitive the UE. It consists of looking for event topology — encoded in event shape observables — for which the effect of jets from the hard subprocess to the usual observables sensitive to the UE is minimal. We perform a generator level study to identify the topology of events, for which the toward region is less sensitive to the extra jets.

### 4.1.1 Event simulation and selection

Four different sets of $Z$-boson events decaying into muon pairs, $Z \to \mu^+\mu^-$, at a centre-of-mass energy of $\sqrt{s} = 13$ TeV are used in this study. Two MC event generators are used to generate the events. For each event generator, two different settings were used one with MPI on and the another with MPI off.

Pythia8 [51] is used to generate events at leading order (LO). It is configured with

the Monash tune [46] using the NNPDF2.3LO [47] parton distribution function (PDF). The MPI is simulated using the *Sjöstrand-van Zijl* model [52], and the hadronization process is performed using the *Lund string hadronization model* [53].

Madgraph 2.5.5 [44] is used to generate $Z$-boson events with up to 3 extra jets (multileg). The other parton level processes — MPI and BR— as well as the showering and hadronization processes are performed by Pythia8 using the MLM matching scheme [45] with value of *xqcut* of 30 GeV.

### 4.1.2 Definition of the observables

In this study, event shape observables and UE observables are constructed using primary charged particles excluding the muon pairs produced from the decay of the Z-boson. These are charged particles with a mean lifetime $\tau > 300$ ps. They are either produced directly from the parton level interactions or from the subsequent decays of particles with a lifetime $\tau < 30$ ps. Charged particles are used instead of the all final state particles so that particle level results can be compared to detector level and real date measurements. In fact, the ATLAS detectors are only able to individually reconstruct charged particles. Charged particles are also required to have $p_T > 0.5$ GeV and $|\eta| < 2.5$. Even though this study is performed at generator level, these cuts are motivated by the design of the ATLAS detector.

#### 4.1.2.1 Underlying event observables

As mentioned previously, the sensitivity to the UE of the toward region in $Z$-boson events is the goal of this study. The charged particles located in this region is used to define the following two infrared sensitive observables.

- The charged particles multiplicity density , $N_{Chg}/\delta\eta\delta\phi$, or multiplicity density represents the number of charged particles in the toward region for one event normalized to per unit of $\eta-\phi$. The mean of the sum of the transverse momentum density is defined as <sum $p_T$ density>:=$< \sum p_T/\delta\eta\delta\phi >$.

- The sum of transverse momentum density, $\sum p_T/\delta\eta\delta\phi$, represents of the sum of transverse momentum of charged particles in the toward region for one event

normalized per unit of $\eta - \phi$. The mean multiplicity density is defined as $< N_{Chg}$ density$>:=< N_{Chg}/\delta\eta\delta\phi >$.

#### 4.1.2.2 Event shape observables

In hadron colliders, event shapes are observables that incorporate the distribution of the flow of the energy for an event. Event shape observables in $Z$-boson events have been measured by CMS [32] and ATLAS [27]. Two of the most commonly used event shape observables are used for this study.

First, we have the transverse thrust $T$ or thrust, which is defined as [38, 39]:

$$T = \max_{\vec{n}_T} \frac{\sum_i \mid \vec{p}_{T,i} \cdot \vec{n}_T \mid}{\sum_i p_{T,i}}, \tag{4.1}$$

where $i$ stands for all charged particles in the final state, and $\vec{n}_T$ is the thrust axis which maximizes the sum. Values of thrust lie in the range of $[2/\pi, 1]$, with $T = 1$ for pencil-like event and $T = 2/\pi$ for spherical event. The thrust axis is found using the algorithm implemented in [50] where it is iterated from a starting direction $\vec{n}_T^{(0)}$ according to

$$\vec{n}_T^{(j+1)} = \frac{\sum_i \epsilon \left( \vec{n}_T^{(j)} \cdot \vec{p}_{T,i} \right) \vec{p}_{T,i}}{\mid \sum_i \epsilon \left( \vec{n}_T^{(j)} \cdot \vec{p}_{T,i} \right) \vec{p}_{T,i} \mid} \tag{4.2}$$

where $\epsilon(x) = 1$ for $x > 0$ and $\epsilon(x) = -1$ for $x < 0$.

While the transverse sphericity $S$ or sphericity is defined as [38]:

$$S = \frac{\pi^2}{4} \min_{\vec{n}=(n_x,n_y,0)^T} \left( \frac{\sum_i \mid \vec{p}_{T,i} \times \vec{n} \mid}{\sum_i p_{T,i}} \right)^2, \tag{4.3}$$

where the summation is over all charged particles $i$, and $\vec{n}$ is an azimuthal vector that minimizes the sum. Pencil-like events have a sphericity around $S = 0$, whereas spherical events have a sphericity close to $S = 1$. According to [38], the vector $\vec{n}$ coincides with one of the transverse momentum vectors $p_{T,i}$ of the charged particles.

The algorithm used for computing these two observables follows the one implemented in Rivet (Robust Independent Validation of Experiment and Theory) [48].

### 4.1.3 Analysis and results

Results shown here are the study of the activity of charged particles in the toward region. For a $Z$-boson events, let us recall that HS, MPI, BR and ISR (there is no gluon

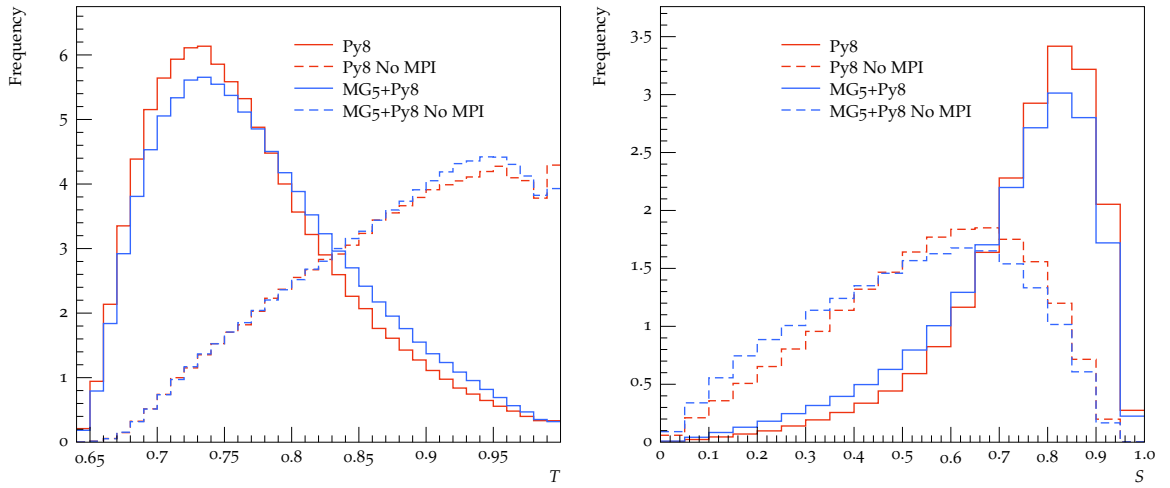



Figure 4.3: Transverse thrust $T$ (left) and transverse sphericity $S$ (right) distribution, both with MPI on and off for LO and multileg setups.

FSR) are the sources of particles in the final state. The differences between the four sets of events —Pythia8 with MPI on and off, and Madgraph with MPI on and off— can be used to deduce the average contribution of each of these processes. Pythia8 with MPI off represents the contribution of the BR and the ISR in the toward region. Madgraph5+Pythia8 with MPI off can be interpreted as the contribution of the fraction of particles produced from the BR, the ISR and the extra jets. The average contribution of the extra jets in the toward region is represented by the difference between Pythia8 with MPI off and Madgraph5+Pythia8 with MPI off. And the average contribution of charged particles produced through MPI for Pythia8 (Madgraph5+Pythia8) is the difference between Pythia8 (Madgraph5+Pythia8) for MPI on and MPI off.

#### 4.1.3.1 Thrust and sphericity distributions

The distribution of the thrust, $T$, and the sphericity, $S$, are shown in Figure 4.3. It shows that events are more likely to be isotropic. Comparing distributions for MPI on and off, it is deduced that MPI makes an event to be isotropic. Such observation is normal since the particles sensitive to HS process — particles produced via HS itself, and particles balancing the momentum of HS — have to be back-to-back.

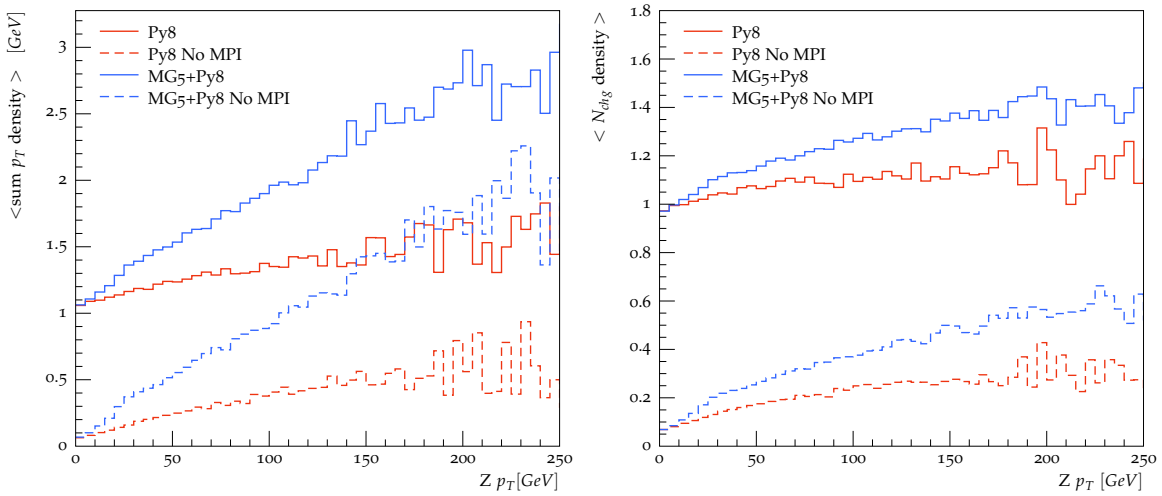



Figure 4.4: The mean of the sum of the transverse momentum density <sum $p_T$ density> (left), and the mean of the multiplicity density < $N_{Chg}$ density> (right) of charged particles in the toward region as a function of the momentum the $Z$-boson $Z_{p_T}$, both with MPI on and off for Pythia8 and Madgraph+Pythia8.

#### 4.1.3.2 Charged particles activity in the toward region as a function of the transverse momentum of the $Z$-boson $p_T^Z$

The mean of the sum of the transverse momentum density, <sum $p_T$ density>, and the mean of multiplicity density, < $N_{Chg}$ density>, of charged particles in the toward region are studied as a function of the $Z$-boson transverse momentum, $p_T^Z$, as shown in Figure 4.4. The average MPI contribution in the toward region is roughly constant with respect to the $Z$-boson momentum $p_T^Z$ for Pythia8 and for Madgraph+Pythia8. In addition, the MPI contribution for Pythia8 and Madgraph+Pythia8 are almost the same. Thus the difference seen in the activity of charged particles in the toward region between Pythia8 and Madgraph+Pythia8 can be then only explained by the contributions of the ISR and the BR, and the ISR, the BR and the extra jets respectively. Comparing Pythia8 with MPI off —contribution of the ISR and the BR— to Madgraph5+Pythia8 with MPI off —contribution of the ISR, the BR and the extra jets—, one can deduce that the extra jets contribution in the toward region increases with the momentum of the $Z$-boson. This increase of the extra jets activity with the momentum of the $Z$-boson explain the increase of the difference in the activity of charged particles between the two MC event generators.

#### 4.1.3.3 Charged particles activity in the toward region as a function of the thrust $T$ and the sphericity $S$

The mean of the sum of the transverse momentum density, <sum $p_T$ density>, and the mean of the multiplicity density, $< N_{Chg}$ density>, of charged particles in the toward region are studied as a function of the thrust $T$, as shown in Figure 4.5. Dijet-like event has a high value of sphericity $S$, whereas spherical event has a low value of sphericity $S$.

For Pythia8 and Madgraph+Pythia8 both with MPI off, the <sum $p_T$ density> and the $< N_{Chg}$ density> are mostly flat with a constant extra charged particles activity from Madgraph+Pythia8. It shows that the effect of the extra jets on the charged particles in the toward region is independent of the topology of event using thrust $T$.

For the two MC event generators, the charged particles activity in the toward region decreases with the values of the thrust $T$. It means that events with more charged particles in the toward region are more likely to be spherical, while events with less charged particles in the toward region are more likely to be dijet-like.

The <sum $p_T$ density> decreases slowly with the value of the trust $T$ for Madgraph+Pythia8 compared to Pythia8, whereas the $< N_{Chg}$ density> decreases at roughly the same rate for two MC event generators. It can be deduced that Pythia8 and Madgraph+Pythia8 produce roughly the same amount of charged particles through MPI, but those produced in Madgraph+Pythia8 carry higher transverse momentum than those produced in Pythia8.

The mean of the sum of the transverse momentum density, <sum $p_T$ density>, and the mean of the multiplicity density, $< N_{Chg}$ density>, of charged particles in the toward region are studied as a function of the sphericity $\mathcal{S}$, as shown in Figure 4.6. Dijet-like event has a low value of sphericity $S$, whereas spherical event has a high value of sphericity $S$.

The MPI contribution to the <sum $p_T$ density> is roughly constant for Madgraph+Pythia8, whereas it increases with the values of the sphericity $S$ for Pythia8. For the MPI contribution to the $< N_{Chg}$ density>, the two MC event generators presents the same behavior. The $< N_{Chg}$ density> increases from dijet-like event to spherical events. It implies that Madgraph+Pythia8 generates less particles with high

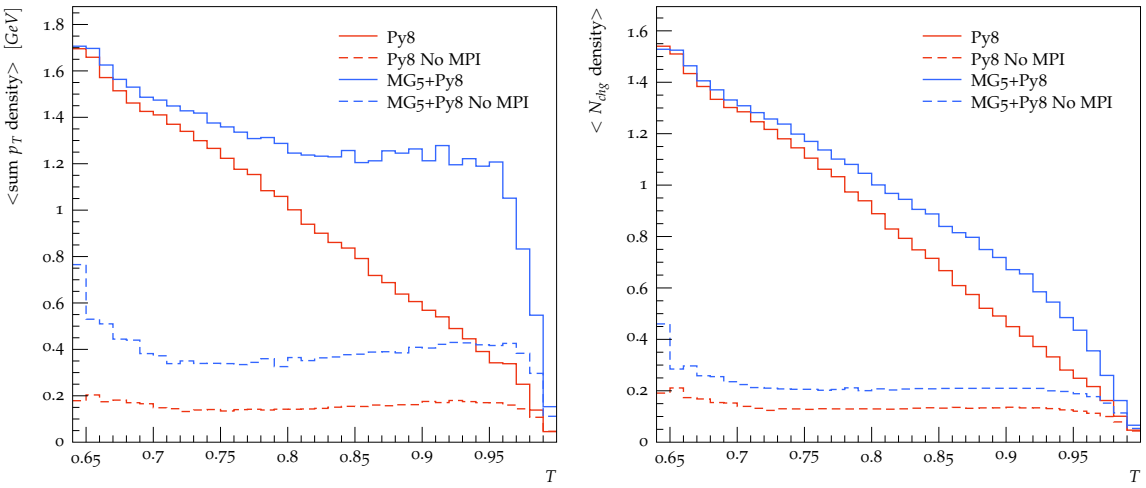



Figure 4.5: The mean of the sum of the transverse momentum density <sum $p_T$ density> (left), and the mean of the multiplicity density < $N_{Chg}$ density> (right) of charged particles in the toward region as a function of the the thrust $T$, both with MPI on and off for Pythia8 and Madgraph+Pythia8.

momentum for dijet-like event and more particles with low momentum for spherical event to keep constant the MPI contribution to the <sum $p_T$ density>.

For Pythia8 and Madgraph+Pythia8 with both MPI off, the <sum $p_T$ density> and < $N_{Chg}$ density> decreases with the values of the sphericity $S$. In addition, the difference between the predictions from these two MC event generators with MPI off decreases also with the sphericity $S$. It means that the toward region is more likely to be contaminated by the extra jets and ISR for dijet-like events than the spherical events.

Pythia8 and Madgraph+Pythia8 present two very different curves for the <sum $p_T$ density>. For events generated with Pythia8, it increases with the value of the sphericity $S$, while the opposite happens for Madgraph. While the < $N_{Chg}$ density> increases with the value of the sphericity $S$ for both Pythia8 and Madgraph+Pythia8. In addition, a disagreement is shown between the prediction of these two MC event generators for dijet-like events, whereas they have roughly the same prediction for spherical events.

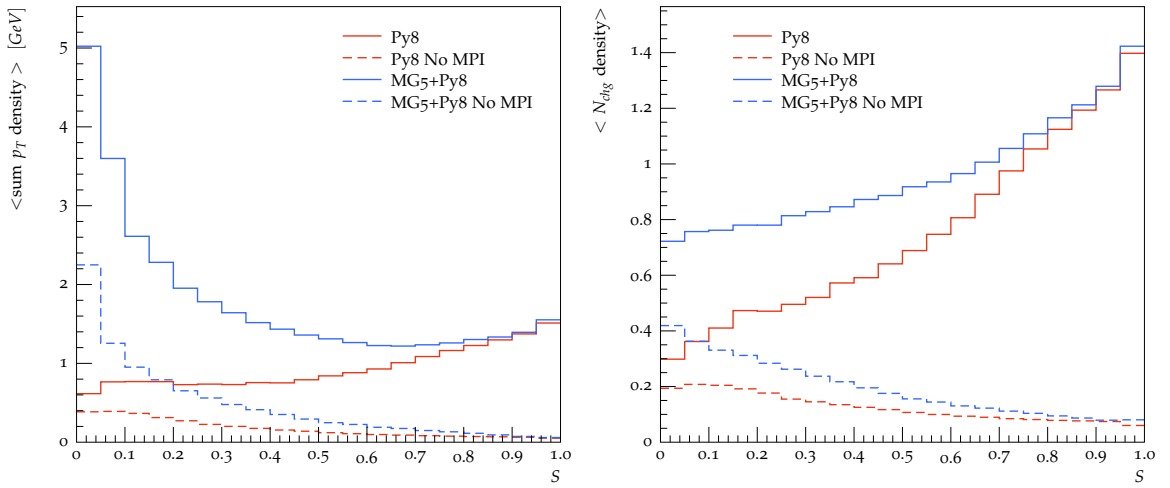



Figure 4.6: The mean of the sum of the transverse momentum density <sum $p_T$ density> (left) and the mean of the multiplicity density < $N_{Chg}$ density> (right) of charged particles in the toward region as a function of the sphericity $S$, both with MPI on and off for for Pythia8 and Madgraph+Pythia8.

### 4.1.4 Conclusion

The important observation that can be made from Figure 4.5 and Figure 4.6 is, that the mean of the sum of the transverse momentum density <sum $p_T$ density> and the mean of the multiplicity density < $N_{Chg}$ density> of charged particles in the toward region are the same for spherical events. Both Pythia8 and Madgraph+Pythia8 give the same prediction even though Madgraph+Pythia8 is configured to produce more extra jets. It means that the charged particles activity in the toward region for spherical events is insensitive to jets contaminating this region. From these results, the charged particles properties in the toward region for a spherical $Z$-boson event — events with thrust $T < 0.75$, or sphericity $S > 0.65$ — constitute a more cleaner observables —less sensitive to the ISR —to constrain the modelling of MPI and BBR.

## 4.2 Measurement of observables sensitive to the underlying event in $t\bar{t}$ events at $\sqrt{s} = 13$ TeV

Improvement in the modeling of soft-QCD parton level interactions in $t\bar{t}$ events has become crucial to perform precise measurement of $t$-quark properties in proton-proton collision. In fact, the main source of uncertainty in these $t$-quark properties measurements comes from the modeling of these soft-QCD interactions. Measurements of observables sensitive to the UE in $t\bar{t}$ events are then needed to constrain the modeling of these interactions in MC event generators. The measurements can be used to verify the accuracy of the event generators to model the data, and to improve models by tuning the simulation to data.

Study of the UE in $t\bar{t}$ dimuon decay channel, $t\bar{t} \to WbW\bar{b} \to \mu^+\nu b\mu^-\nu\bar{b}$, using the data collected by the ATLAS detector is the focus of the present work. The measurements are performed in $t\bar{t}$ events, in the dileptonic channel using muons, as it presents a cleaner final state compared to any semi-leptonic and any all-hadronic channels. In fact, the two $b$-quarks from the decay of the $t$- and $\bar{t}$-quark, are the only unavoidable sources of FSR for the dileptonic channel. Whereas, the final state of the semi-leptonic and the all-hadronic channels involves four to six quarks, that are all possible sources of QCD radiation. And the dimuon decay channel is preferred to the other dileptonic channels due to the efficiency of the ATLAS detector for the muon reconstruction.

A first study of the UE in $t\bar{t}$ events has been performed by the CMS collaboration in proton-proton collisions at $\sqrt{s} = 13$ TeV [33]. It uses the traditional transverse plane method to define region with strong sensitivity to the UE. Whereas the same approach as in Section 4.1 is used in the present work. It consists of looking for event topology, for which the effect of jets to the trans-min region — which is defined using the usual transverse plane method — is minimal. This section is organized as follows. Section 4.2.1 describes the data and simulated events used in this work. Object reconstruction and identification method at the detector and particle level are described in Section 4.2.2. The methodology and the results are shown in Section 4.2.4 and Section 4.2.5 , respectively.

### 4.2.1 Data and MC simulation samples

#### 4.2.1.1 Measured data

The data used for the present measurement were collected by the ATLAS detector in 2015 and 2016. It consists of proton-proton collision delivered by the LHC at $\sqrt{s}$ = 13 TeV with a 25 ns bunch spacing. Out of the 39.5 fb$^{-1}$ data recorded by the ATLAS detector, data collected under stable beam conditions and requiring the all subdetectors to be operational are only considered. This includes the 3.2 fb$^{-1}$ and 32.9 fb$^{-1}$ data recorded respectively in 2015 and 2016, which corresponds to a total integrated luminosity of 36.1 fb$^{-1}$. During these data taking periods, the average number of inelastic proton-proton collision per bunch crossing $< \mu >$ for 2015 and 2016 data are respectively 13 and 24.5.

#### 4.2.1.2 Monte Carlo simulation samples

At the stage of the present work, the background contributions are not yet considered, sample of simulated events are used for the unfolding procedure and to perform comparison with data.

The unfolding procedure requires both the knowledge of the measured value of the observable at truth and detector level [81]. Measured value of an observable at truth or particle level refers to the quantity measured using directly the output of the MC event generators. Whereas, measured value of an observables at detector level refers to the quantity measured using the reconstructed object from the simulation of the interactions between the detector and the particles produced from the MC event generators.

Only the $t\bar{t}$ signal sample is generated, that is used for the unfolding procedure and to perform comparison with the data. The $t\bar{t}$ sample was generated using Powheg-Box [60, 61, 62], Pyhtia8 [51], and EvtGen [63]. Powheg-Box was used to generate the matrix elements of the $t\bar{t}$ production at next-to-leading order (NLO) in the strong coupling constant $\alpha_S$, using the NLO parton distribution function NNPDF3.0 [65]. Pythia8 with the A14 [66] tune using the leading order (LO) parton distribution function NNPDF2.3 [64] was used to simulate the UE. In addition, the showering of the partons produced from the primary interactions, and their successive fragmentation

and hadronization are further processed with Pythia8. The $h_{damp}$ parameter which controls the transition from the matrix element to the parton shower, is set to be $h_{damp} = 1.5 \cdot m_{top}$, where the mass of the $t$-quark $m_{top}$ is 172.5 GeV. Futhermore, the decay of the heavy-flavour hadrons — $c$-hadrons and $b$-hadrons —, is simulated using EvtGen. The GEANT4 [68] simulation toolkit is used to simulate the interaction between the ATLAS detector [67] with the simulated events. The same reconstruction method as for the real data, is applied after the detector simulation.

### 4.2.2 Object reconstruction and identification

For $t\bar{t}$ events in dimuon decay channel, the final state consists of two muons, at least two jets initiated by $b$-quark and neutrinos. The reconstructions of these particles at detector and particle level are described in this section.

#### 4.2.2.1 Detector level reconstruction

**Primary vertex** Tracks are first reconstructed using the information in the ID, as described in [70]. A collection of vertices are then reconstructed from the reconstructed tracks. The primary vertex is considered as the vertex with the highest sum of the transverse momentum of its associated tracks [69].

**Muons** Muons and anti-muons leave tracks in the ID as well as in the MS when traversing the ATLAS detector. In addition, as an electrically charged leptons, muons may also lose energy when traversing the ECAL despite their low ionising property. The reconstruction of the ID and MS tracks, as well as the energy deposited in the ECAL are performed independently. The details of their reconstruction in the ATLAS detector can be found in [72] and [73].

Four different types of muons —*combined*, *segment-tagged*, *calorimeter-tagged*, and *extrapolated* muon— can be reconstructed using different combinations of the information from the ID, MS and ECAL [72]. The reconstruction of the combined and segment-tagged muons are based on the information in ID and MS. Calorimeter-tagged muons use the ID and ECAL information in their reconstruction algorithm. Extrapolated muons are reconstructed using only information in the MS. The first three types of muons use the ID tracks in their reconstruction algorithm, which could lead to the

reconstruction of two or three muons sharing the same ID track. In this case, priority is given to the combined muon, followed by the segment-tagged muon, and finally to the calorimeter-tagged muon. For reconstructed muons sharing the same MS tracks, priority is given to the reconstructed muon using track with better fit quality and larger number of hits.

The reconstructed muons can be either prompt muons, or muons produced from the pion and kaon decays. Muon identification and isolation selections are criteria applied on these reconstructed muons to reduce the background contamination and to have a robust momentum measurement. In the present work, muons candidate are required to satisfy the so-called `Medium` muon identification and `Gradient` muon isolation criteria as defined in [72]. In addition, muons are required to be within $|\eta| < 2.5$ and to have $p_T > 25$ GeV.

**Jets** Due to the confining nature of QCD, quarks and gluons cannot be directly measured, only the bunch of colorless particles resulting from their fragmentation and hadronization, referred to as jet, are experimentally accessible. However it is experimentally impossible to identify each of the particles induced by the parton to infer its properties. In addition, there is no defined rule derived from theory, that dictates the clustering of particles to form a jet. Based on the physics intent, different types of jets can be defined depending on the *input objects* — the collection of objects on which the jet is reconstructed —, and the *jet clustering algorithm* with its possible parameters.

The standard ATLAS jet definition is used in the present work. It uses the anti-$k_t$ algorithm [41] with radius parameter $R = 0.4$ as the jet clustering algorithm, and the three dimensional mass-less and positive energy topological clusters [74, 75] as input objects. The FastJet package [40] was used to do the reconstruction. These input objects are clusters of hadronic calorimeter cell energies. The clustering algorithm uses the topology of the position of each of the cell signals to establish connection between neighbors cells. Cell with an energy below a noise threshold is discarded in order to reject calorimeter electronic noise and pile-up contamination. Jets are required to be within $|\eta| < 2.5$ and to have $p_T > 25$ GeV.

Jets initiated by a $b$-quark, from here referred to as $b$-jets, have properties that

can be used to distinguish them for the other jets. In fact, the decay products of a $b$-hadron tend to have a smaller mass compared to the $b$-hadron mass. As a result, $b$-jets tend to be wider with more constituents compared to the other jets. In addition, $b$-hadrons have a longer mean life time than any other hadrons. Thus they can travel some distance before decaying, which will result as a reconstructible secondary vertex. The multivariate discriminant `MV2c10` is the $b$-tagging algorithm that is used in the present work. Details on the `MV2c10` $b$-tagging algorithm can found in [76, 77, 78].

**Missing transverse energy** Neutrinos traverse the ATLAS detector without interacting with any subdetectors material. They don't leave any tracks in the ID or deposit any energy in the calorimeters. Their properties can not be then measured directly. However, the momentum transverse to the two colliding protons is known to be zero, which implies that the net transverse momentum of the final state particles should be also equal to zero. A momentum imbalance, referred to as *missing transverse energy* $\overrightarrow{E}_T^{miss}$, implies the presence of undetectable particles, neutrinos in our case. The $\overrightarrow{E}_T^{miss}$ is defined as:

$$\overrightarrow{E}_T^{miss} = -\overrightarrow{E}_T^{miss,hard} - \overrightarrow{E}_T^{miss,soft}.$$

The hard term $\overrightarrow{E}_T^{miss,hard}$, represents the vector sum of the transverse momentum of all calibrated physics objects, which are the reconstructed jets and muons in our case. And the soft term $\overrightarrow{E}_T^{miss,soft}$, represents the vector sum of the transverse momentum of any signal not associated to the hard term.

The magnitude $E_T^{miss}$, and azimuthal angle $\phi^{miss}$ of $\overrightarrow{E}_T^{miss}$ are respectively:

$$E_T^{miss} = \sqrt{(E_x^{miss})^2 + (E_y^{miss})^2},\ and$$
$$\phi^{miss} = arctan(E_y^{miss}/E_x^{miss}).$$

**Overlap removal** When applied, the reconstruction procedure described before could lead to the reconstruction of two different objects using the same detector information. In this case, an overlap removal is applied, which consists of rejecting one of the two objects. In the present work, muon is discarded if it is within a $\Delta R < 0.4$ from any jets in order to reduce non-prompt muon contamination.

#### 4.2.2.2 Particle level object reconstruction

**Muons** In order to ensure that the particle level muons are produced from an electroweak process, they are required to not originate from hadron decays. All photons within $\Delta R = 0.1$ of a muon candidate, and not originating from any hadron decays are considered as its photon radiation. The four-momenta of the muon candidate is modified by adding the four-momenta of these photons. In addition, these muon candidates are required to be within $|\eta| < 2.5$ and to have $p_T > 25$ GeV.

**Jets** Jets are reconstructed using the same jet clustering algorithm as for the detector level. All stable final state particles, except leptons and neutrinos not originating from hadron decays, as well as their photon radiations are used as jet inputs. Jets are required to be within $|\eta| < 2.5$ and to have $p_T > 25$ GeV. The ghost matching technique as described in [42], is used for the $b$-jet tagging.

**Missing transverse energy** The particle level missing transverse energy $E_T^{miss}$, is defined as the vector sum of the transverse momentum of neutrinos not originating from hadron decays, either directly or through a $\tau$ decay.

### 4.2.3 Event selection

First, events are required to pass a single muon trigger with low $p_T$ thresholds of 25 GeV for 2015 data and a single muon trigger with low $p_T$ thresholds of 27 GeV for 2016 data. Then the following conditions are required for each event to be considered. Events are required to have exactly two muons of opposite sign with $p_T > 25$ GeV and within $|\eta| < 2.5$. Furthermore, their invariant mass, $m_{inv}^{\mu^+\mu^-}$, is required to be $m_{inv}^{\mu^+\mu^-} > 15$ GeV, but should not be between 80 GeV and 100 GeV which is the $Z$-boson peak. Events are required to have at least two jets within $|\eta| < 2.5$ and with $p_T > 25$ GeV, with at least one of them must be $b$-tagged. The missing transverse energy is required to be $E_T^{miss} > 60$ GeV.

### 4.2.4 Methodology

For $t\bar{t}$ events in dimuon decay channel , the leading direction for the transverse plane method, is considered as the vector sum of the transverse momentum of the $t\bar{t}$ system,

$\overrightarrow{p}_T^{t\bar{t}}$, which is defined as:

$$\overrightarrow{p}_T^{t\bar{t}} = \overrightarrow{p}_T(jets) + \overrightarrow{p}_T(muons) + \overrightarrow{E}_T^{miss},$$

where $p_T(jets)$, $p_T(muons)$, and $E_T^{miss}$ refer respectively to the vector sum of the all reconstructed jets, the vector sum of the two muons, and the missing transverse energy. The sensitivity to either the hard interaction or the UE of the three azimuthal regions in the transverse plane for $t\bar{t}$ events in the dimoun decay channel is as follows. The away region as usual contains particles balancing the momentum of the $t\bar{t}$, thus it is more sensitive to the $t\bar{t}$ system. For the toward region, as the dimuon $t\bar{t}$ final state involves at least two colored partons, this region is more likely to be contaminated by QCD radiation from these partons. The toward region has then a strong sensitivity to the hard interaction. The transverse region is the region with the lowest sensitivity to the hard interaction, as it is by construction perpendicular to the $t\bar{t}$ system.

#### 4.2.4.1 Definition of the observables

The same event shape and the UE observables defined in Section 4.1.2.2 and Section 4.1.2.1 are also used in the present work. In addition, we also use the mean transverse momentum of charged particles defined as $\sum p_T/N_{Chg}$, which represents the average momentum of the charged particle per event. Event shape and UE observables are reconstructed using charged particles excluding the muon pairs.

For the detector level, charged particle is reconstructed as track in the ID. Each reconstructed track is required to have $p_T > 0.5$ GeV and within $|\eta| < 2.5$. In addition, in order to get a good track quality, each track is required to have at least one hit in the inner most pixel layer, at least one hit in the pixel detector, and at least 6 SCT hits. For a track with $p_T > 10$ GeV, its fit probability $\chi^2$ must be greater than 0.01 in order to suppress mis-measured tracks. To reduce the pile-up contribution, their transverse impact parameter measured with respect to the LHC beam line, $d_0$, and their longitudinal impact parameter measured with respect to the primary vertex, $z_0$, are required to satisfy $|d_0| < 1.5$ mm and $|z_0|sin\theta < 1.5$ mm. In order to exclude the muon ID tracks, tracks within $\Delta R < 0.2$ from the two reconstructed muons are discarded.

For the particle level, charged particle are required to have $p_T > 0.5$ GeV and

within $|\eta| < 2.5$. Primary stable charged particles are those with a `status code` $= 1$.

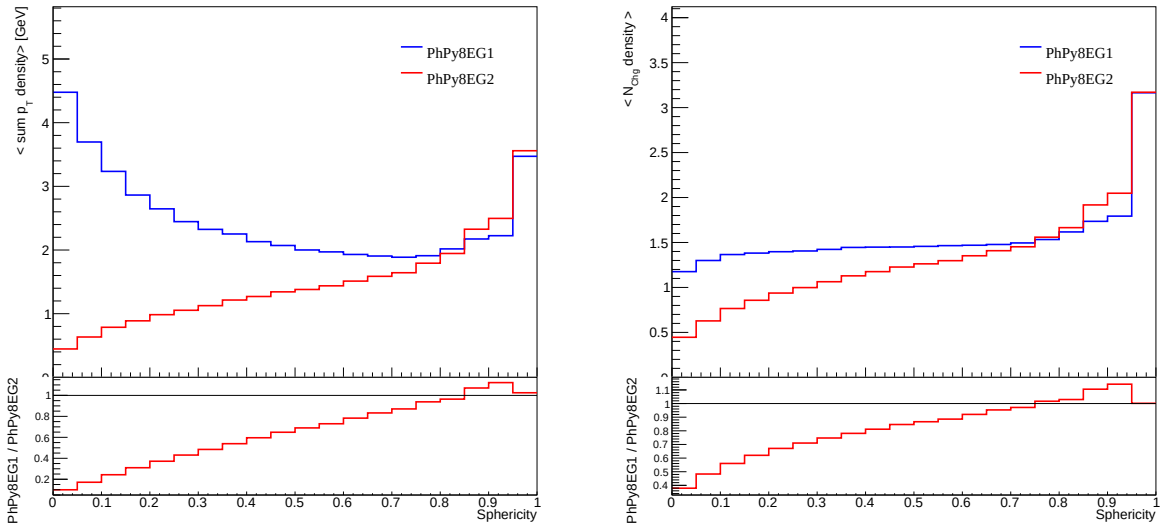
#### 4.2.4.2 Particle level study of the sensitivity of the trans-min region to jets

In a proton-proton collision, the final state of the partonic level interactions consists of partons from the showering of the final state of the hard interaction, and partons contributing to the UE. At the current energy scale reached by the LHC, partons contributing to the UE can be also reconstructed as jets. In addition, it is experimentally impossible to identify, if a jet is induced by a parton from either the hard interaction or the MPI. Thus, the requirement of an observable to be less sensitive to the collection of reconstructed jets, reduces the sensitivity of the observable to the hard interaction.

In this section, we perform a particle level study to identify event topology, for which the trans-min region is not sensitive to the reconstructed jets. Using the MC sample described in Section 4.2.1.2, two different sets of event are considered. The first set of events, referred to as *PhPyEG1* from now, consists of events passing the cut flow defined in Section 4.2.3. Whereas, the second set of events, referred to as *PhPyEG2* from now, consists of events passing the cut flow defined in Section 4.2.3, and they are further required that no reconstructed jets are located in their transverse region.

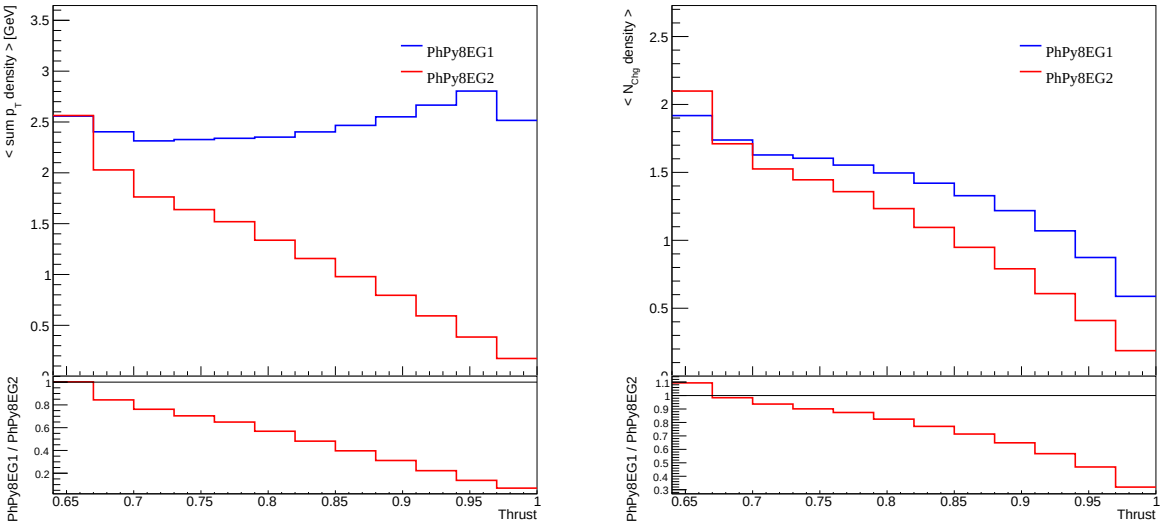
The study of the mean of the sum of the transverse momentum density, <sum $p_T$ density>, and the mean of the multiplicity density, $< N_{Chg}$ density>, of charged particles in the trans-min region as function of the sphericity $S$ is shown in Figure 4.7. For the value of sphericity $S > 0.75$, the <sum $p_T$ density> and the $< N_{Chg}$ density> are the same for these two types of events. Thus for spherical events i.e events with $S > 0.75$, the trans-min region is insensitive to jets.

The study of the mean of the sum of the transverse momentum density, <sum $p_T$ density>, and the mean of the multiplicity density, $< N_{Chg}$ density>, of charged particles in the trans-min region as function of the thrust $T$ is shown in Figure 4.8. For the value of thrust $T < 0.7$, the <sum $p_T$ density> and the $< N_{Chg}$ density> are the same for these two types of events. Thus for spherical events i.e events with $T < 0.7$, the trans-min region is insensitive to jets.




(a) (b)

Figure 4.7: The mean of (a) the sum of the transverse momentum density <sum $p_T$ density>, and (b) the mean of the multiplicity density $< N_{Chg}$ density> of charged particles in the trans-min region as a function of the spherocity $S$. Two types of events were considered: for all events shown in blue, and for events for which the trans-min region is not contaminated by any jets, shown in red.




(a) (b)

Figure 4.8: The mean of (a) the sum of the transverse momentum density <sum $p_T$ density>, and (b) the mean of the multiplicity density $< N_{Chg}$ density> of charged particles in the trans-min region as a function of the thrust $T$. Two types of events were considered: for all events shown in blue, and for events for which the trans-min region is not contaminated by any jets, shown in red.

### 4.2.5 Results

The results presented in this work will focus on the measurement of the properties of charged particles in the transverse. region with a more emphasis on the trans-min region as it is expected to be less sensitive to the HS. Measured data are unfolded to particle level using the bin-by-bin unfolding method [81].

#### 4.2.5.1 Comparison between the transverse, the trans-max and the trans-min region

Comparisons of the measured mean of the sum of the transverse momentum density <sum $p_T$ density>, and the mean of the multiplicity density $< N_{Chg}$ density> of charged particles in the trans-min, trans-max and transverse region as a function of the $p_T^{t\bar{t}}$ are shown in Figure 4.9. These two variables measured in the trans-min region show a small dependence on the $p_T^{t\bar{t}}$, as they are roughly constant for any value of $p_T^{t\bar{t}}$ up to 140 GeV, where they start rising gently. In contrast, the <sum $p_T$ density> measured in the trans-max and in the transverse region show a dependence on the $p_T^{t\bar{t}}$. In fact, a tendency to increase with the value of $p_T^{t\bar{t}}$ is noticed as shown in Figure 4.9(a). As already mentioned in Section 4.1, this can be explained by the fact that the trans-max region receive contribution by the extra-jets from the HS.

#### 4.2.5.2 Comparison between the trans-min region for spherical and dijet-like events using the sphericity S

Comparisons of the measured mean of the sum of the transverse momentum density <sum $p_T$ density>, the mean of the multiplicity density $< N_{Chg}$ density> , and the mean of mean of the transverse momentum <mean $p_T$ > of charged particles in the trans-min region for spherical ($S > 0.75$) and dijet-like event ($S \leq 0.75$) using sphericity as a function of the $p_T^{t\bar{t}}$ are shown in Figure 4.10. For the $< N_{Chg}$ density>, both spherical and dijet-like event present roughly the same behavior with respect to the $p_T^{t\bar{t}}$. In fact, they both fluctuate around 1.2 for any value of $p_T^{t\bar{t}}$. However for <sum $p_T$ density>, spherical and dijet-like events show two different profiles. The <sum $p_T$ density> for spherical events is constant for any value of the $p_T^{t\bar{t}}$, which means that it

is insensitive to any contamination by the HS. While the <sum $p_T$ density> for pencil-like events increases with the value of $p_T^{t\bar{t}}$, which implies that it receive contribution from the $t\bar{t}$ system.

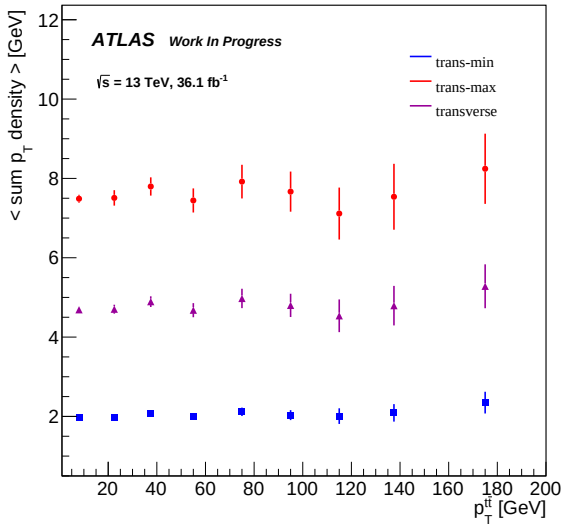
#### 4.2.5.3 Comparison between the trans-min region for spherical and dijet-like events using the thrust T

Comparisons of the measured mean of the sum of the transverse momentum density <sum $p_T$ density>, the mean of the multiplicity density $< N_{Chg}$ density> , and the mean of mean of the transverse momentum <mean $p_T$ > of charged particles in the trans-min region for spherical ($T < 0.7$) and dijet-like event ($T \leq 0.7$) using sphericity as a function of the $p_T^{t\bar{t}}$ are shown in Figure 4.10. For the $< N_{Chg}$ density>, both spherical and dijet-like event present roughly the same behavior with respect to the $p_T^{t\bar{t}}$. In fact, they both fluctuate around 1.2 for any value of $p_T^{t\bar{t}}$. The <sum $p_T$ density> for spherical and dijet-like events increase at the same rate with the value of $p_T^{t\bar{t}}$. However, the <sum $p_T$ density> for spherical event is always lower compared to the dijet-like event.

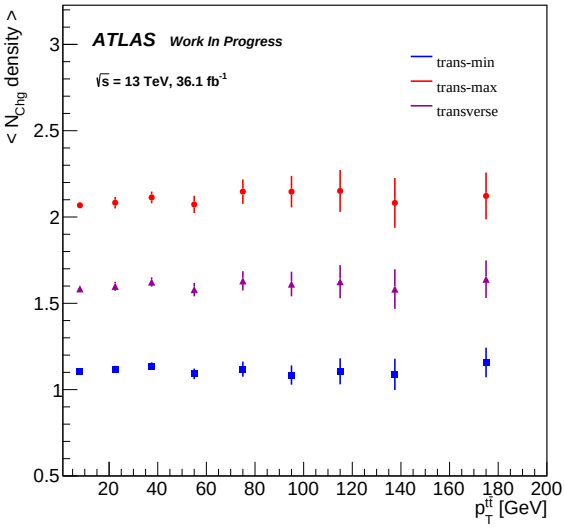
#### 4.2.5.4 Comparison of distribution of UE observables between the MC sample and the data

The MC predictions at particle level are compared to the unfolded data for the normalized distributions of the sum of transverse momentum density $\sum p_T/\delta\phi\delta\eta$, and the charged particles multiplicity $N_{Chg}/\delta\phi\delta\eta$. The MC event generator fails to describe the data for spherical as well as for dijet-like events. In general, the MC event generator predicts less events with low value of $\sum p_T/\delta\phi\delta\eta$, and $N_{Chg}/\delta\phi\delta\eta$ compared to the measured data.

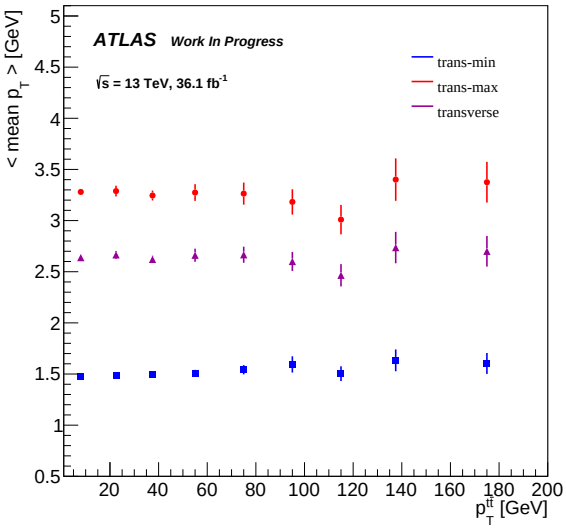
For dijet-like events defined with sphericity and thrust, shown in Figure 4.12 and Figure 4.14, the measured data and the simulation favors events with low $\sum p_T/\delta\phi\delta\eta$, and $N_{Chg}/\delta\phi\delta\eta$. Whereas for spherical events defined with the sphericity and thrust, shown in Figure 4.13 and Figure 4.15, the distributions of $\sum p_T/\delta\phi\delta\eta$, and $N_{Chg}/\delta\phi\delta\eta$ for the measured data and the simulation all have the same shape. The distributions all have one peak around 1.5 for both the value of $\sum p_T/\delta\phi\delta\eta$, and $N_{Chg}/\delta\phi\delta\eta$.




(a)

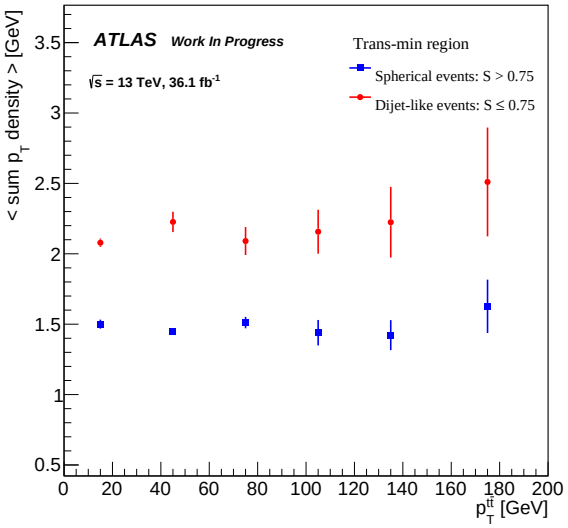



(b)

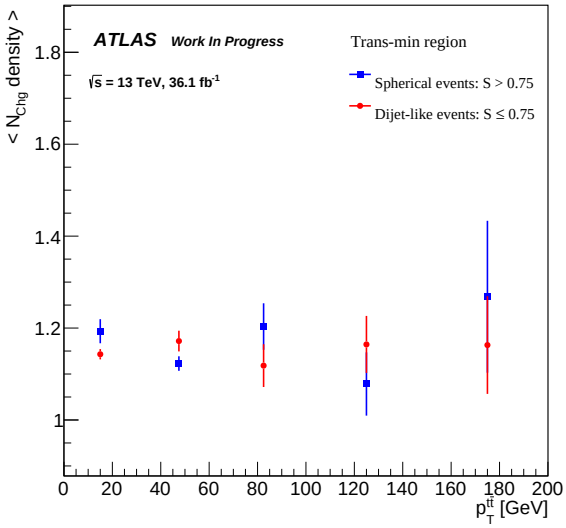



(c)

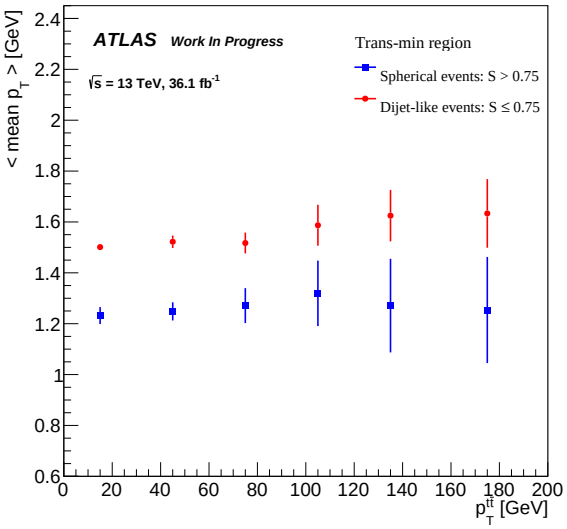
Figure 4.9: (a) The mean of the sum of the transverse momentum density <sum $p_T$ density>, (b) the mean of the multiplicity density < $N_{Chg}$ density>, and (c) the mean of the mean transverse momentum <mean $p_T$ >, of charged particles in the trans-min, trans-max and transverse region as a function of the $p_T^{t\bar{t}}$.




(a)

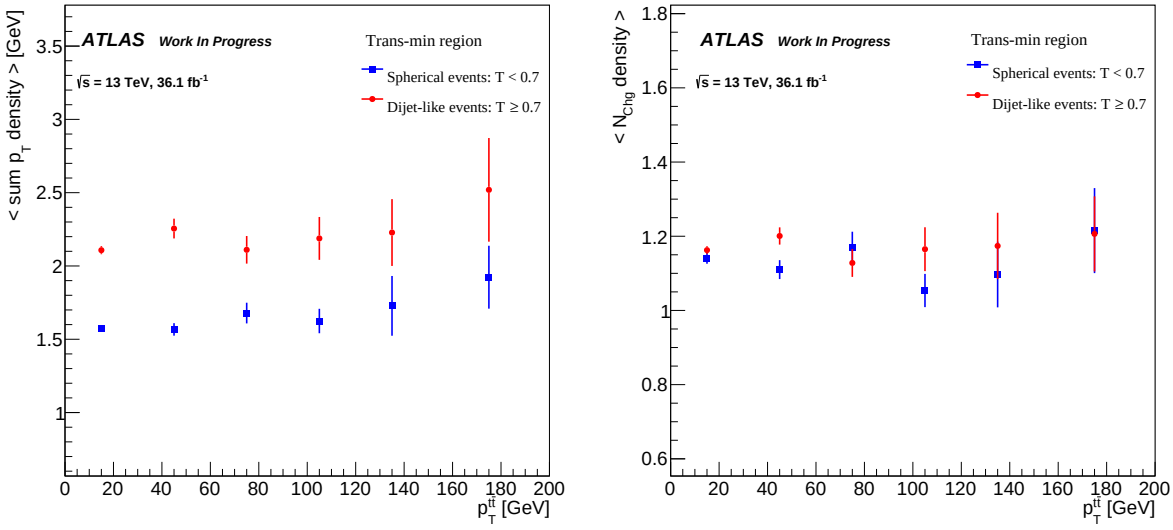



(b)




(c)

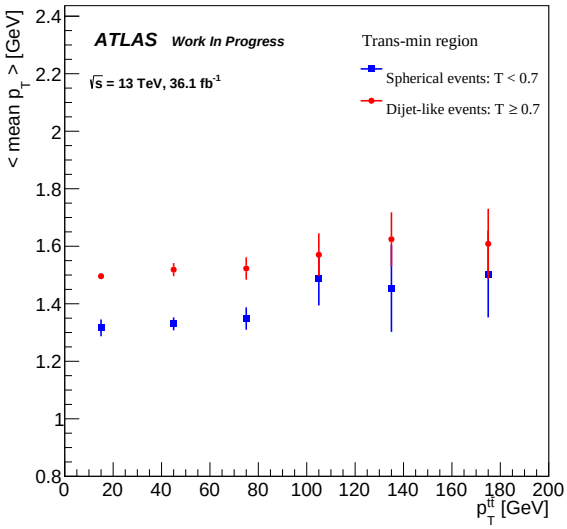
Figure 4.10: (a) The mean of the sum of the transverse momentum density <sum $p_T$ density>, (b) the mean of the multiplicity density $< N_{Chg}$ density>, and (c) the mean of the mean transverse momentum <mean $p_T$ >, of charged particles in the trans-min region for $S > 0.75$ and for $S \leq 0.75$ as a function of the $p_T^{t\bar{t}}$.




(a)

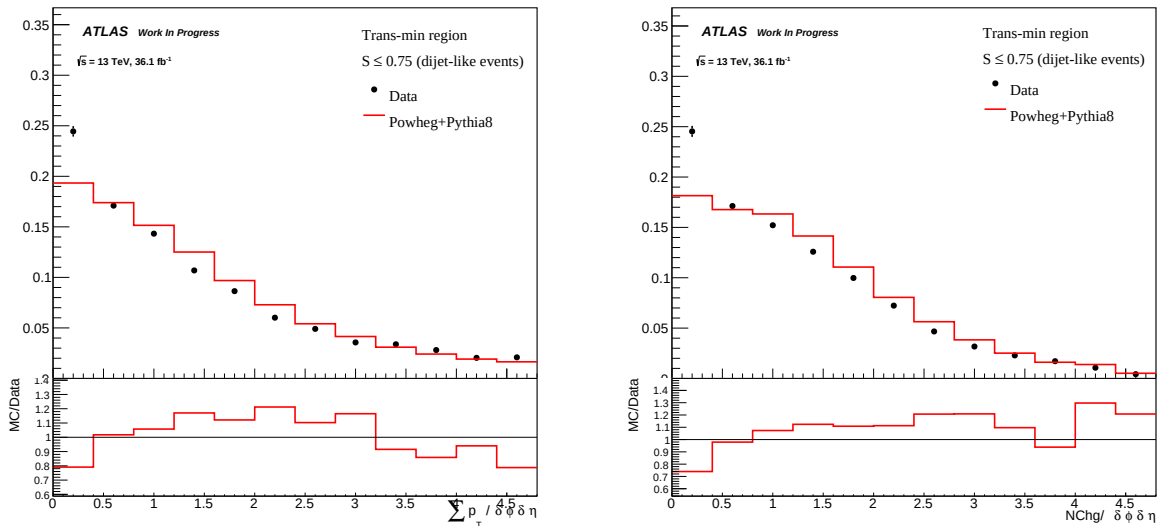



(b)



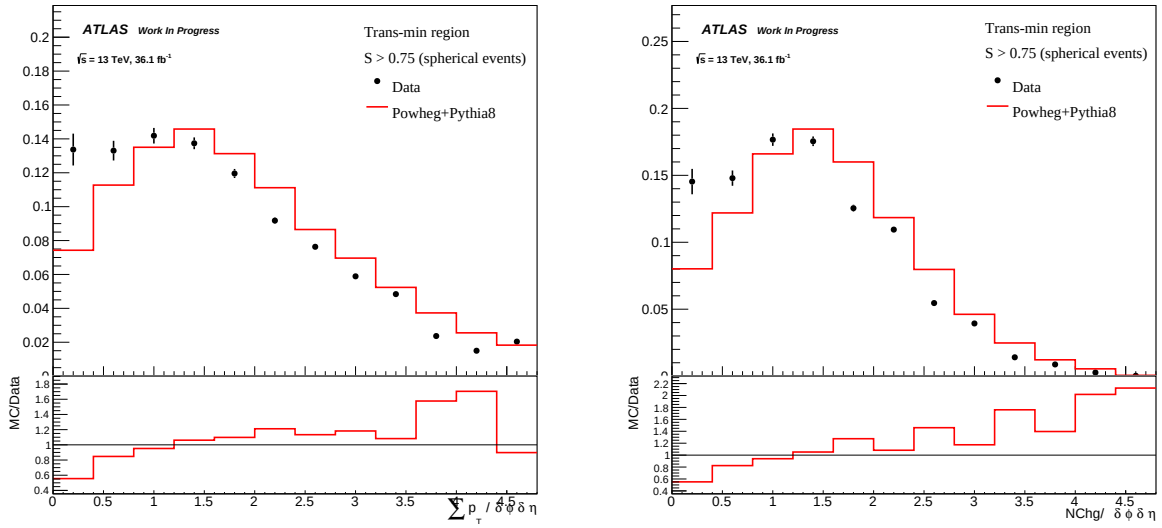

(c)

Figure 4.11: (a) The mean of the sum of the transverse momentum density <sum $p_T$ density>, (b) the mean of the multiplicity density $< N_{Chg}$ density>, and (c) the mean of the mean transverse momentum <mean $p_T$ >, of charged particles in the trans-min for $T < 0.7$ and for $T \geq 0.7$ as a function of the $p_T^{t\bar{t}}$.



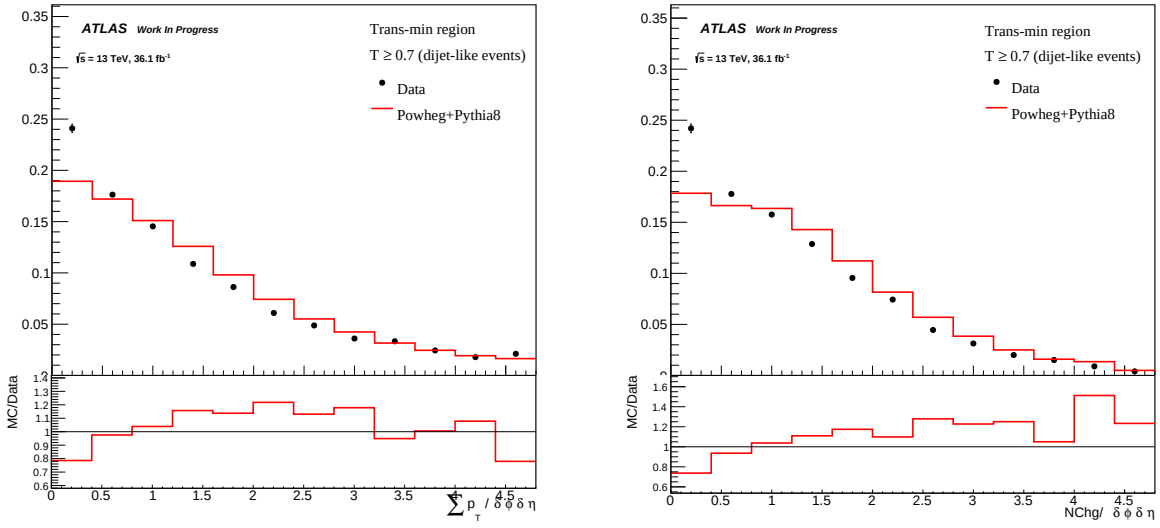

(a) (b)

Figure 4.12: Distribution of (a) the sum of the transverse momentum density of charged particles$\sum p_T/\delta\phi\delta\eta$, and (b) the charged particles multiplicity density $N_{Chg}/\delta\phi\delta\eta$ for events with $S \leq 0.75$.



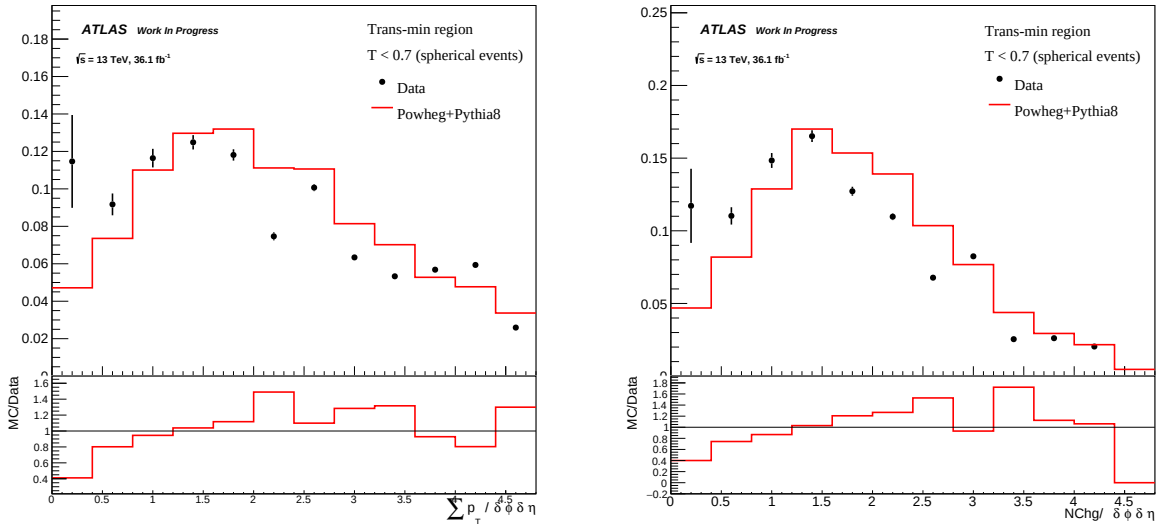

(a) (b)

Figure 4.13: Distribution of (a) the sum of the transverse momentum density of charged particles$\sum p_T/\delta\phi\delta\eta$, and (b) the charged particles multiplicity density $N_{Chg}/\delta\phi\delta\eta$ for events with $S > 0.75$.




(a) (b)

Figure 4.14: Distribution of (a) the sum of the transverse momentum density of charged particles$\sum p_T/\delta\phi\delta\eta$, and the (b) charged particles multiplicity density $N_{Chg}/\delta\phi\delta\eta$ for events with $T \geq 0.7$.



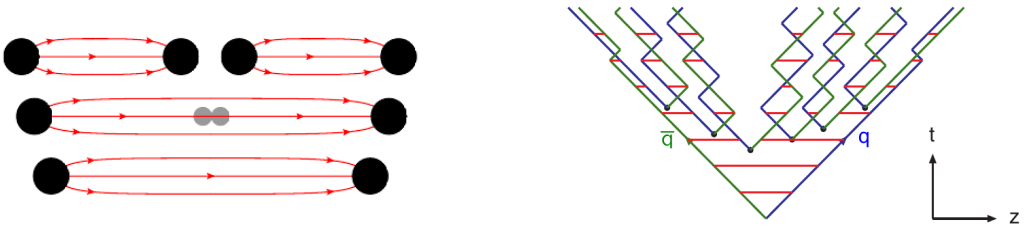

(a) (b)

Figure 4.15: Distribution of (a) the sum of the transverse momentum density of charged particles$\sum p_T/\delta\phi\delta\eta$, and (b) the charged particles multiplicity density $N_{Chg}/\delta\phi\delta\eta$ for events with $T < 0.7$.

# Chapter 5

# Study of the color reconnection in all hadronic $t\bar{t}$ events

In the Lund string model [53], the gluon field formed between a color dipole $q\bar{q}$ is modeled as a string like color field. The strengh of this gluon field increases with the distance between the color charge, such that when the dipole moves apart from each other, $q'\bar{q}'$ pair creation and annihilation can occur inside this region in space. When the energy stored in this stringlike color field is enough to produce $q_0\bar{q}_0$ pair, the string breaks to produce two new dipoles $q\bar{q}_0$ and $q_0\bar{q}$ as shown in Figure 5.1(a). These two color-singlet systems can undergo the same process again and again. Such mechanism is illustrated in Figure 5.1(b), where only the time and one space coordinate are shown.




(a) (b)

Figure 5.1: Illustration of (a) the string breaking by quark pair creation in the string field, and (b) the motion and breakup of a string system, with the two transverse degrees of freedom suppressed (diagonal lines are (anti)quarks, horizontal ones snapshots of the string field) [20].

In a proton-proton collision, the final state of the partonic level interactions consists of partons from the showering of the final state of the hard interaction, and partons from the UE. The flow of the color charges in each subsequent evolution of these partons is described by the CR picture, where quark and gluon of one color are connected to quark and gluon of the corresponding anti-color by a string color field. The flow of color charge in QCD vertices is shown in Figure 5.2.



Figure 5.2: QCD color propagation rules for elementary quark-gluon and triple gluon vertex. The black lines represent the Feynman diagram and the colored lines represents the color propagation rule [1].

Since there is no first principle model that can be used to describe CR, one can only use QCD inspired models to describe the mechanism of this string field. However, due to the lack of observables that can be used to constrain these models, the modeling of CR is one of the main source of uncertainty in many measurements of the $t$-quark properties. In fact, the reconstruction of the decay product of the $t$-quark is sensitive to the modeling of CR, as the $q\bar{q}$ from the $W$-boson decay are color connected.

## 5.1 Aim

Measurements of color reconnection using the jet pull angle in $t\bar{t}$ events in proton-anti-proton at $\sqrt{s} = 1.96$ TeV [57], and in proton-proton at $\sqrt{s} = 8$ TeV [58] were performed by the DØ and ATLAS experiment respectively. The sensitivity to CR of the jet pull angle — observables reconstructed using jet constituents, that quantify the orientation of radiation inside one jet relative to another — was measured in these two works, but the results were not able to significantly distinguish singlet and octet radiation patterns in jets.

The present work focus on the study of the sensitivity to CR of jet superstructure. More precisely, we probe if the CR mechanism affects the properties of final state particles between a pair of jets. In fact, we expect that the $q\bar{q}$ produced from the fragmentation of the string like color fields between two color connected jets, would enhance the production of particles between them. A difference on the properties of

final state particles between a pair of color connected jets, and a pair of non color connected jets implies, that the final state particles production located between two jets is sensitive to the CR mechanism.

## 5.2 Methodology

Event with a known color composition of its final state is required for such measurement. In addition, its final state has to have at least one pair of singlet color connected partons and one parton color connected to the background (MPI and BBR), so that one can make a comparison between a pair of color connected jets and two pairs of non color connected jets. The all hadronic $t\bar{t}$ channel, $t\bar{t} \rightarrow W\bar{b}Wb \rightarrow q\bar{q}'\bar{b}q\bar{q}'b$, is known to have such a final state. In fact, the $q\bar{q}'$ from the decay product of the $W$-bosons are known to be singlet color connected, whereas the $b$-quark is known to be color connected to the background. A Feynman diagram of a $t\bar{t}$ all hadronic channel is shown in Figure 5.3, where colored lines represent the string like color fields between two color connected objects.

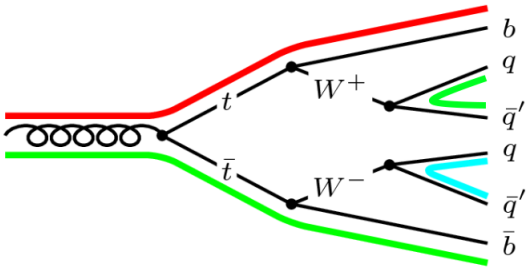



Figure 5.3: Feynman diagram of a $t\bar{t}$ all hadronic channel (black lines) with QCD color propagation rule (colored lines).

The all boosted hadronic channel is chosen for this study, as it reduces a combination complexity to assign the production of each reconstructed jets to the $t$-quark, the $\bar{t}$-quark decay product, or to the background. In fact, for a high transverse momentum $t$-quark ($\bar{t}$-quark) referred to as boosted $t$-quark ($\bar{t}$-quark), its decay products will be collimated, that they will be contained in a jet with radius parameter $R = 1.0$. This large radius jet can be considered as jet initiated by the $t$-quark, and the subjets — reconstructed jets with a smaller radius parameter $R = 0.2$ — inside the large radius jet can be considered as the jets initiated by the decay product of $t$-quark. Figure 5.4

illustrates a large radius jets, shown as the black circle, with its three subjets shown as the three red circles.

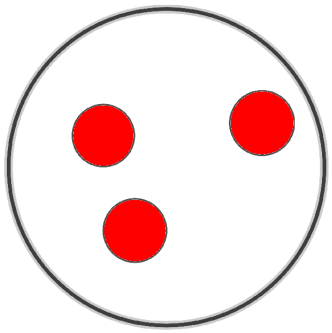


Figure 5.4: A representation of a large radius jet (black circles) with its subjets (red circle) in the $\eta - \phi$ plane.

For each possible pairs of subjets inside a large radius jet, we measure the properties of charged particles inside a rectangular region between each pair. The following observables reconstructed from these charged particles are used for this study:

- the charged particles multiplicity density, $N_{Chg}/\delta\eta\delta\phi$, or multiplicity density represents the number of charged particles inside the rectangular region between the two jets normalized by the area of the region,

- and the sum of the transverse momentum density, $\sum p_T/\delta\eta\delta\phi$, represents of the sum of transverse momentum of charged particles inside the rectangular region between the two jets normalized by the area of the region.

For each pair of jets, we define a rectangular region between them as shown illustrated by Figure 5.5. For two jets of radius $r$ and with centers $C1$ and $C2$, the rectangular region between them is built as follows:

- the side $AD$ is perpendicular to the line passing through the centers of the two jets, and its length is equal to $AD = 2r$,

- and the side $AB$ is parallel to the line passing through the centers of the two jets, and its length is equal to $AB = C1C2 - 2r$.

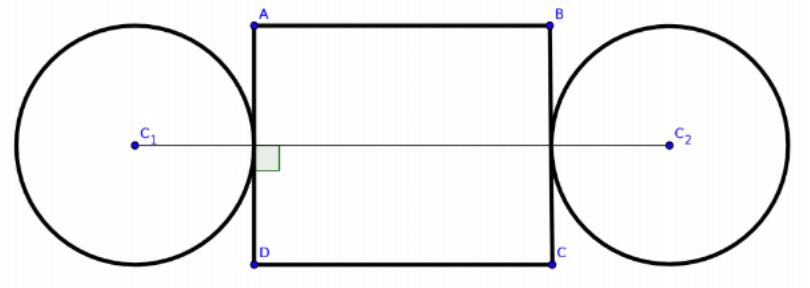



Figure 5.5: Diagram illustrating the rectangular region between jets.

## 5.3 Event simulation and selection

Pythia8 was used to generate 10 million of $t\bar{t}$ events at a centre-of-mass energy of $\sqrt{s} = 13$ TeV. Its setup follows the same as in section 4.1.1. The default Pythia8 color reconnection model was used [51], which is an intermediate in character between [52] and [55]. The $t\bar{t}$ are produced from $q\bar{q}$ annihilation, $q\bar{q} \to t\bar{t}$, or $gg$ annihilation, $gg \to t\bar{t}$. The following cuts are applied on these events to select all boosted $t\bar{t}$ hadronic channel. Events are required to have:

- at least two anti-$k_t$ $R = 1.0$ jets with a $p_T > 200$ GeV considered as the two large jets initiated by the $t$-quark and the $\bar{t}$-quark: they are reconstructed from final state particles with $|\eta| < 4.5$ using the anti-$k_t$ algorithm with radius parameter $R = 1.0$ [41],

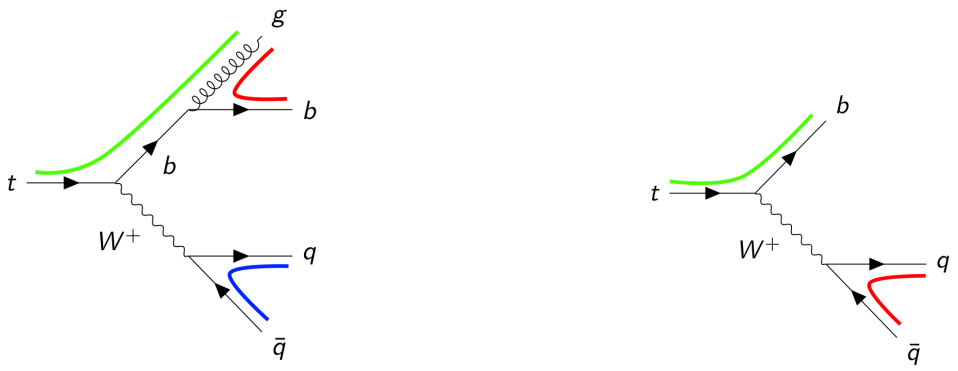
- at least six anti-$k_t$ $R = 0.2$ jets with a $p_T > 25$ GeV: they are reconstructed from final state particles with $|\eta| < 4.5$ using the anti-$k_t$ algorithm with radius parameter $R = 0.2$ [41],

- and at least two of the anti-$k_t$ $R = 0.2$ jets with a $p_T > 25$ GeV are $b$-tagged: the ghost association procedure [42] was used for $b$-jet tagging.

## 5.4 Methodology and results

When a $t$ ($\bar{t}$) quark decays hadronically, at least three quarks are produced, and additional gluons might also be emitted from these quarks. For example, a gluon might be radiated by the $b$-quark as it is shown in Figure 5.8(a). Due to the confining nature of QCD, one can only see jets initiated by these quarks and gluons. However,

depending on the jet algorithm and its possible parameters, and the cut applied on the jets, not all these partons would be reconstructed as jets.




(a) (b)

Figure 5.6: Feynman diagrams (black lines) of a $t$-quark decaying (a) with and (b) without additional radiative gluon from the $b$-quark, where the QCD color propagation rule are shown as the colored lines.

The distribution of the number of reconstructed anti-$k_t$ $R = 0.2$ jets with $p_T > 25\ GeV$ inside an anti-$k_t$ $R = 1.0$ jets with $p_T > 200$ GeV is shown in Figure 5.7. An anti-$k_t$ $R = 0.2$ jet is considered as a subjet of anti-$k_t$ $R = 1.0$ jet, if it is within a distance of $\Delta R < 0.5$ from the anti-$k_t$ $R = 1.0$ jet. In this work, only an anti-$k_t$ $R = 1.0$ jet with three or four anti-$k_t$ $R = 0.2$ jets with one of them b-tagged are considered. It would reduce the number of background for an experimental measurement, and a good statistic is still achieved as most of the large radius jets have such a number of subjets as it is shown in Figure 5.7. They are treated independently, where section 5.4.1 deals with the anti-$k_t$ $R = 1.0$ jet with three subjets, and section 5.4.2 deals with the anti-$k_t$ $R = 1.0$ jet with four subjets.

### 5.4.1 For a large radius jet with three subjets

For a large radius jets with three subjets, the following cuts are further applied. The large radius jet is required to have exactly one $b$-tagged jet, it would also avoid us a combination complexity. For example, if there are two $b$-tagged jets in the large radius, one cannot know which $b$-jet is initiated by the $b$-quark from the direct $t$-quark decay. In addition, it is required that the 3 regions between the 3 pairs of jets, can all be defined as shown in Figure 5.8(a). In fact, for some cases the jet cones of the

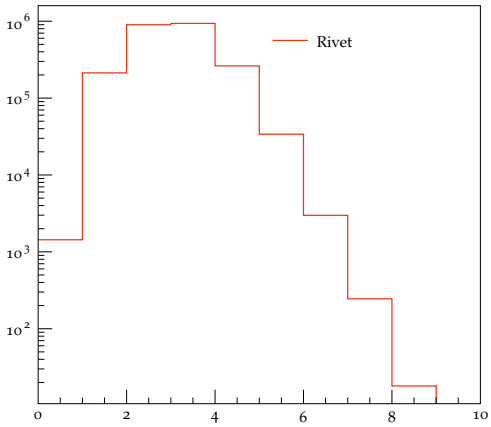
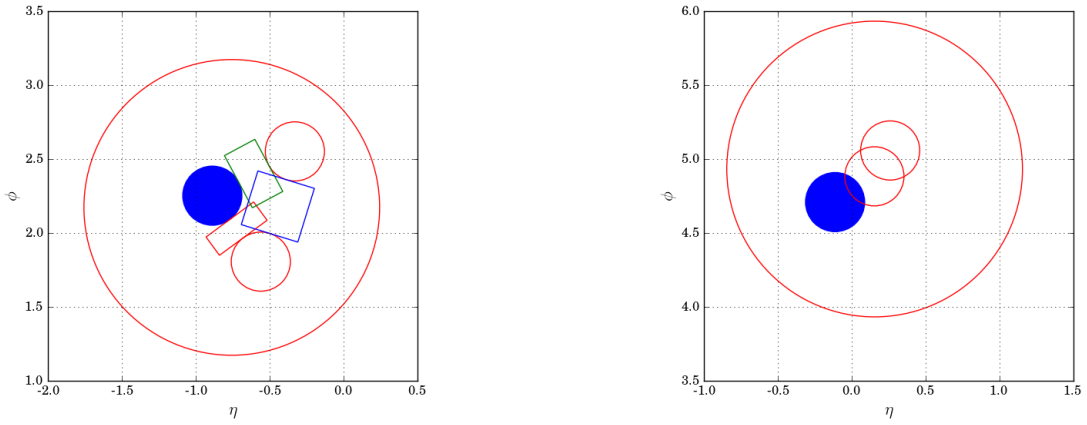



Figure 5.7: Distribution of the number of reconstructed anti-$k_T$ $R = 0.2$ jets with $p_T > 25$ GeV inside an anti-$k_T$ $R = 1.0$ jets with $p_T > 200$ GeV.

subjets inside of some large radius overlap in $\eta - \phi$ plane as shown in Figure 5.8(b), then the rectangular region cannot be defined.




(a) (b)

Figure 5.8: Examples of configurations of anti-$k_t$ $R = 0.2$ jets inside an anti-$k_t$ $R = 1.0$ jet. (a) A large radius jet where the three rectangular areas between the three anti-$k_t$ $R = 0.2$ jets can all be deifned. (b) A large radius jet where jet cones of the three anti-$k_t$ $R = 0.2$ jets overlap.

For a jet with a radius $R = 1$ with exactly three reconstructed subjets of radius $R = 0.2$ where one of them is $b$-tagged, there are 2 possible cases that leads to such configuration.

- The three quarks from the decay of $t$-quark — the $b$-quark and the $q\bar{q}'$ from the decay of the $W$-boson — are all reconstructed as anti-$k_t$ $R = 0.2$ jets. In this

case, the pair of two non b-jets is color connected, and the other two pairs that can be formed from the b-jet with one of the non $b$-jet are not color connected.

- The $b$-quark, one of the $W$-boson decay products, and one radiative gluon from the $b$-quark are reconstructed as anti-$k_t$ $R = 0.2$ jets. In this case, the gluon jet and the $b$-jet are color connected, and the other two pairs that can be formed from the $b$-jet or the gluon jet with the non b-jet are not color connected.

However, only $b$-tagging methods are still the only accepted jet flavor tagging in the field of experimental physics. No standard methods are yet established to distinguish jet initiated by quark to jet initiated by gluon. Thus, one cannot know if the two non $b$-jets are initiated by the $q\bar{q}'$ from the $W$-boson decay, or from the gluon emitted by the $b$-jet and one of the $q\bar{q}'$ from the $W$-boson decay. In this study, we consider that the two non $b$-jets are all from the $W$-boson. Thus, three different pairs of jets can be formed from these three subjets: the $b$-jet (Bj), the leading jet (Wj1) and the subleading jet (Wj2) from the $W$-boson decay. The pair formed by the Bj and the Wj1 (Bj-Wj1) and the pair formed by the Bj and the Wj2 (Bj-Wj2) are not color connected, whereas the pair formed by the Wj1 and the Wj2 (Wj1-Wj2) is color connected.

A comparison of the distributions of the sum of the transverse momentum density $\sum p_T/\delta\eta\delta\phi$, and the multiplicity density $NChg/\delta\eta\delta\phi$ of charged particles between these three pairs of jets are shown respectively in Figure 5.9(a) and Figure 5.9(b). A low activity of charged particles is favored for both the region between the pairs of color and non color connected jets. The charged particles activity between the two pairs of non color connected jets — Bj-Wj1 and Bj-Wj2 — are exactly the same. The difference seen between these two pairs of non color connected jets for the high value of these observables is due to limitation in statistics. As expected, charged particles activity is higher in the region between the pair of color connected jets compared to the two pairs of non color connected jets.

### 5.4.2 For a large radius jet with four subjets

For a large radius jets with three subjets, the following cuts are further applied. The large radius jet is required to have exactly one $b$-tagged jet, it is motivated as in Section 5.4.1. For every pair of jets that the rectangular area between them can be defined,

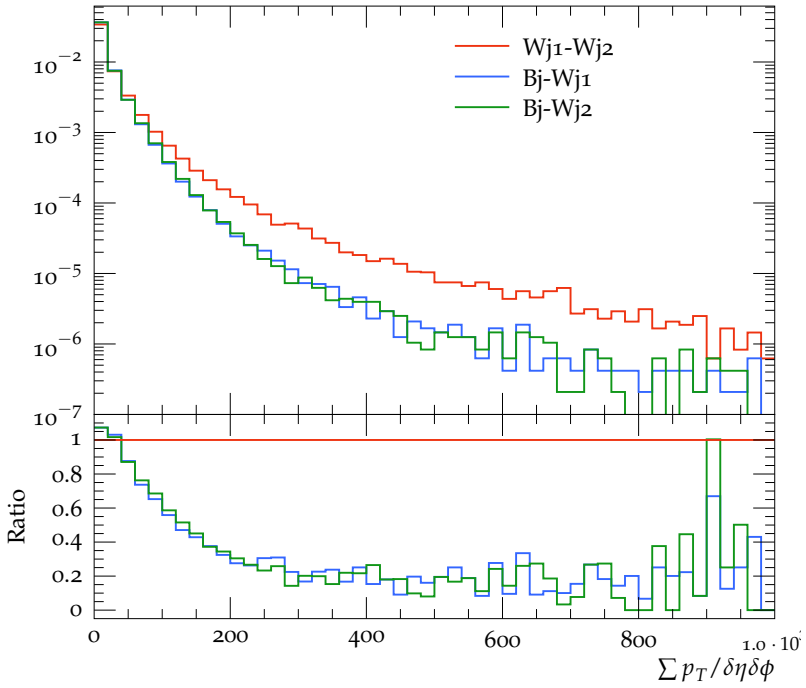
the charged particles activity in that area are measured using the previously defined observables.

For a jet with a radius $R = 1$ with exactly four reconstructed subjets of radius $R = 0.2$ where one of them is $b$-tagged, the three non $b$-jets are considered as initiated by the radiative gluon from the $b$-quark, and the two quarks from the $W$-boson decay. As discussed before, no method are yet capable of identifying if either a given jet is initiated by a quark or a gluon. However, gluons splitting from a colored object are more likely to be emitted with a small angle with respect to the direction of that colored object. By considering that one of the three non $b$-jets is a jet initiated by a gluon emitted by the $b$-quark, we then consider as the gluon jet, the nearest jet to the $b$-tagged jet in the $\eta - \phi$ plane.

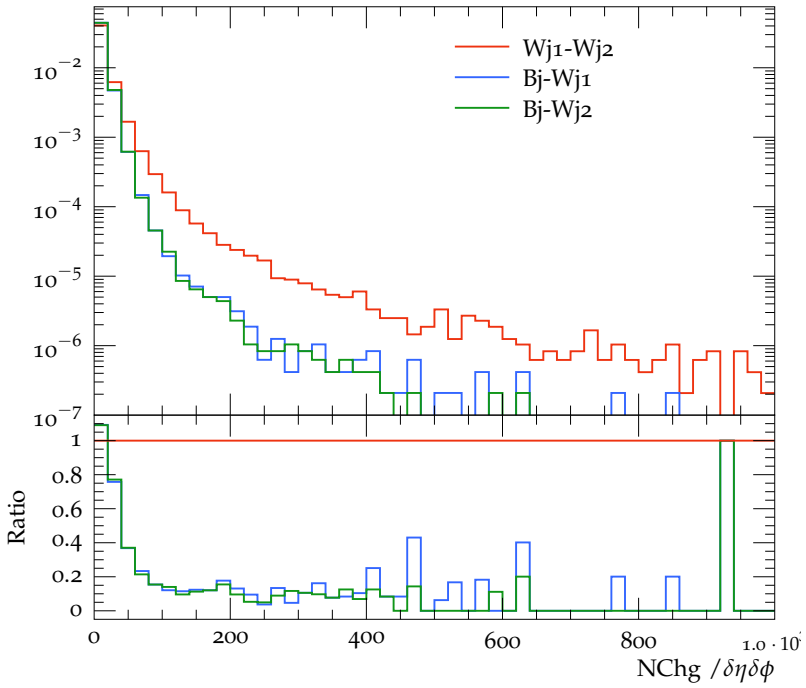
Six different pairs can be formed from these four subjets: the $b$-jet (Bj), the gluon jet (Gj), the leading jet (Wj1) and the subleading jet (Wj2) from the $W$-boson decay. Two pairs of them are color connected: the pair formed by the Wj1 and the Wj2 (Wj1-Wj2), and the pair formed by the Bj and the Gj (Bj-Gj). The other pairs are not color connected: the pair formed by Bj and Wj1 (Bj-Wj1), the pair formed by the Bj and the Wj2 (Bj-Wj2), the pair formed by the Gj and the Wj1 (Gj-Wj1), and the pair formed by the Gj and the Wj2 (Gj-Wj2).

A comparison of the distributions of the sum of the transverse momentum density $\sum p_T/\delta\eta\delta\phi$, and the multiplicity density $NChg/\delta\eta\delta\phi$ of charged particles between these three pairs of jets are shown respectively in Figure 5.10(a) and Figure 5.10(b). A low activity of charged particles is favored for both the region between the pairs of color and non color connected jets. However, the Bj-Wj1 and Bj-Wj2 stand out of the others, as the regions in between these two pairs have the lowest activity of charged particles. The two pairs of color connected jets Wj1-Wj2 and Bj-Gj have a higher charged particles activity compared to the two pairs of non color connected jets Bj-Wj1 and Bj-Wj2. While for the other two pairs of non color connected jets Gj-Wj1 and Gj-Wj2, they do have higher charged particles activity compared to the two pairs of non color connected jets Bj-Wj1 and Bj-Wj2. This could be explained by the fact that the $b$-quark and/or the gluon emitted by the $b$-quark have the same color charge as the $q\bar{q}'$ from the $W$-boson decay, as their color charges are totally independent. Thus, if the $b$-quark/the gluon is close enough to $q\bar{q}'$ from the $W$-boson decay, it is

possible that the string like color fields could be spanned between the $b$-quark/gluon and one the $W$-boson decay. However, there is 1/9 chance that the $b$-quark has the same color as the $q\bar{q}'$ [59], whereas the gluon has a higher chance to have the same color as the $q\bar{q}'$. In fact, it carries two color charge: the same color charge (anti-color) as the $b$-jet and another different color charge.

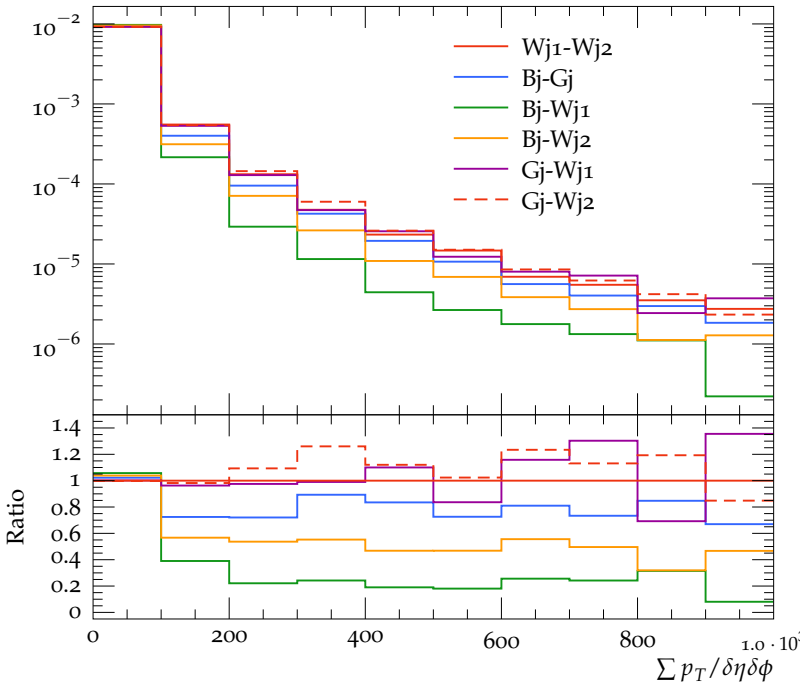



(a)

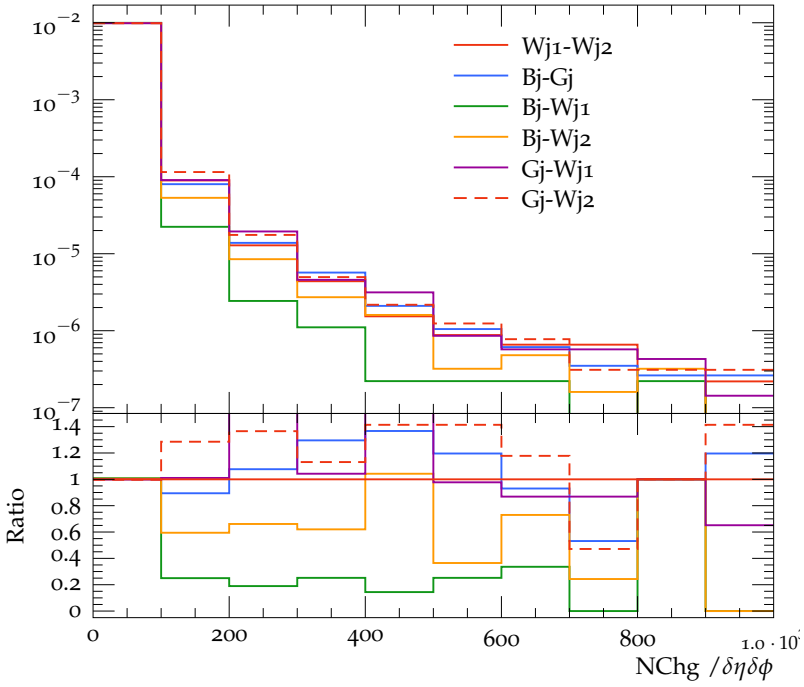



(b)

Figure 5.9: Distributions of (a) the sum of the transverse momentum density $\sum p_T/\delta\eta\delta\phi$, and (b) the multiplicity density $NChg/\delta\eta\delta\phi$ of charged particles between these three pairs of jets. The bottom panel shows the ratio with respect to the pair Wj1-Wj2, where the blue line represents the ratio of the pair Wj1-Wj2 to the pair Bj-Wj1, and the green line represents the ratio of the pair Wj1-Wj2 to the pair Bj-Wj2.




(a)




(b)

Figure 5.10: Distributions of (a) the sum of the transverse momentum density $\sum p_T/\delta\eta\delta\phi$, and (b) the multiplicity density $NChg/\delta\eta\delta\phi$ of charged particles between these six pairs of jets. The bottom panel shows the ratio with respect to the pair Wj1-Wj2, where the blue line represents the ratio of the pair Wj1-Wj2 to the pair Bj-Gj, the green line represents the ratio of the pair Wj1-Wj2 to the pair Bj-Wj1, the orange line represents the ratio of the pair Wj1-Wj2 to the pair Bj-Wj2, the purple line represents the ratio of the pair Wj1-Wj2 to the pair Gj-Wj1, and the dashed red line represents the ratio of the pair Wj1-Wj2 to the pair Bj-Wj2.

# Chapter 6

# Conclusions

The present work was focused on the study of the UE in $Z$-boson events, and in $t\bar{t}$ events in the dimuon decay channel, as well as the CR in $t\bar{t}$ all hadronic decay channel, with boosted top quarks.

For the study of the UE in $Z$-boson events, we find that the toward region, defined using the usual transverse plane method, for spherical events is less sensitive to the hard interaction process. Thus the toward region for spherical events is cleaner to perform measurements of UE.

For the study of the UE in $t\bar{t}$ events in dimuon decay channel, we also find that the trans-min region, defined using the usual transverse plane method, for spherical events is less sensitive to the hard interaction process. In addition, measurements of observables in the trans-min region for spherical and dijet-like events using data collected by ATLAS detector in 2015 and 2016, are compared to the prediction of MC event generator in the $t\bar{t}$ events in dimuon decay. The MC event generator fails to describe the data for any distributions.

For the study of CR in $t\bar{t}$ all hadronic decay channel, with boosted top quarks, we find that observables defined using the properties of the charged particles between a pair of jets shows differences between a pair of color connected and a pair of non color connected jets. Thus these observables are sensitive to CR. However, the difference between the two types of pair of jets is small that might disappear when measured with data.

# Bibliography


[1] C. Patrignani *et al.*, *Review of Particle Physics*, Chin. Phys. C 40.10 (2016), p. 100001. incl. 2017 update.

[2] S. L. Glashow, *Partial Symmetries of Weak Interactions*, Nucl. Phys. **22** (1961) 579.

[3] S. Weinberg, *A Model of Leptons*, Phys. Rev. Lett. **19** (1967) 1264.

[4] A. Salam and J. C. Ward, *Electromagnetic and Weak Interactions*, Phys. Lett. **13** (1964).

[5] P. W. Higgs, *Broken symmetries, massless particles and gauge fields*, Phys. Lett. **12** (1964).

[6] P. W. Higgs, *Broken Symmetries and the Masses of Gauge Bosons*, Phys. Rev. Lett. **13** (1964).

[7] G. S. Guralnik, C. R. Hagen, and T. W. B. Kibble, *Global conservation laws and massless particles*, Phys. Rev. Lett. **13** (1964).

[8] F. Englert and R. Brout, *Broken Symmetry and the Mass of Gauge Vector Mesons*, Phys. Rev. Lett. **13** (1964).

[9] D. J. Gross and F. Wilczek, *Ultraviolet behavior of non-abelian gauge theories*, Phys. Lett. **30** (1973).

[10] H. D. Politzer, *Reliable Perturbative Results for Strong Interactions?*, Phys. Lett. **30** (1973).

[11] CDF Collaboration, *Observation of Top Quark Production in $p\bar{p}$ Collisions with the Collider Detector at Fermilab*, Phys. Rev. Lett. **74** (1995), arXiv: 9503002 [hep-ex].

[12] D0 Collaboration, *Search for High Mass Top Quark Production in $p\bar{p}$ Collisions at $\sqrt{s} = 1.8$ TeV*, Phys. Rev. Lett. **74** (1995), arXiv: 9411001 [hep-ex].

[13] ATLAS Collaboration, *Observation of a new particle in the search for the Standard Model Higgs boson with the ATLAS detector at the LHC*, Phys. Lett. B**716** (2012), arXiv:1207.7214 [hep-ex].

[14] CMS Collaboration, *Observation of a new boson at a mass of 125 GeV with the CMS experiment at the LHC*, Phys.Lett. B**716** (2012), arXiv:1207.7235 [hep-ex].

[15] L. Evans and P. Bryant, *LHC Machine*, JINST 08 (2008), JINST 3 (2008), S08001.

[16] ALICE Collaboration, *The ALICE experiment at the CERN LHC*, JINST 3 (2008), S08002.

[17] ATLAS Collaboration, *The ATLAS Experiment at the CERN Large Hadron Collider*, JINST 3 (2008), S08003.

[18] CMS Collaboration, *The CMS experiment at the CERN LHC*, JINST 3 (2008), S08004.

[19] LHCb Collaboration, *The LHCb Detector at the LHC*, JINST 3 (2008), S08005.

[20] P.Skands, *Introduction to QCD*, TASI 2012, arXiv: 1207.2389 [hep-ph].

[21] Wikipedia, Standard Model, Accessed: June 11, 2019.

[22] CDF Collaboration, *Charged jet evolution and the underlying event in proton-antiproton collisions at 1.8 TeV*, Phys. Rev. **D65**(2002), 092002.

[23] CDF Collaboration, *Underlying event in hard interactions at the Fermilab Tevatron $p\bar{p}$ collider*, Phys. Rev. **D70**(2004), 072002, arXiv: 0404004 [hep-ex].

[24] CDF Collaboration, *Studying the underlying event in Drell-Yan and high transverse momentum jet production at the Tevatron*, Phys. Rev. **D82**(2010), 034001, arXiv: 1003.3146 [hep-ex].

[25] ATLAS Collaboration, *Measurement of distributions sensitive to the underlying event in inclusive Z-boson production in pp collisions at* $\sqrt{s} = 7$ *TeV with the ATLAS detector*, Eur. Phys. J. **C74** (2014) no. 12, 3195, arXiv: 1409.3433 [hep-ex].

[26] ATLAS Collaboration, *Measurement of distributions sensitive to the underlying event in inclusive Z-boson production in pp collisions at* $\sqrt{s} = 7$ *TeV with the ATLAS detector*, Eur. Phys. J. **C74** (2014) no. 12, 3195, arXiv: 1409.3433 [hep-ex].

[27] ATLAS Collaboration, *Measurement of event shape observables in* $Z \to l^+l^-$ *events in pp collisions at* $\sqrt{s} = 7$ *TeV with the ATLAS detector at the LHC*, Eur. Phys. J. C (2016) 76:375, arXiv: 1602.08980 [hep-ex].

[28] CMS Collaboration, *First measurement of the underlying event activity at the LHC with* $\sqrt{s} = 0.9$ *TeV*, Eur. Phys. J. **C70** (2010) 555, arXiv: 1006.2083 [hep-ex].

[29] CMS Collaboration, *Measurement of the underlying event activity at the LHC with* $\sqrt{s} = 7$ *TeV and comparison with* $\sqrt{s} = 0.9$ *TeV*, JHEP **09**(2011) 109, arXiv: 1107.0330 [hep-ex].

[30] CMS Collaboration, *Measurement of the underlying event in the DrellYan process in protonproton collisions at* $\sqrt{s} = 7$ *TeV*, Eur. Phys. J. **C72** (2012) 2080, arXiv: 1204.1411 [hep-ex].

[31] CMS Collaboration, *Measurement of the underlying event activity in inclusive Z boson production in proton-proton collisions at* $\sqrt{s} = 13$ *TeV*, arXiv: 1711.04299 [hep-ex].

[32] CMS Collaboration, *Event shapes and azimuthal correlations in Z + jets events in pp collisions at* $\sqrt{s} = 7$ *TeV*, Phys. Lett. B**722** (2013) 238-261, arXiv: 1301.1646 [hep-ex].

[33] CMS Collaboration, *Study of the underlying event in top quark pair production in pp collisions at 13 TeV*, Eur. Phys. J. C. (2019) 79, arXiv: 1807.02810 [hep-ex].

[34] CDF Collaboration, R. Field, *The Underlying event in hard scattering processes*, eConf **C010630** (2001) P501, arXiv: 0201192 [hep-ph].

[35] G. Marchesini and B. R. Webber, *Associated transverse energy in hadronic jet production*, Phys. Rev. D**38** (1988), 3419.

[36] J. Pumplin, *Hard underlying event correction to inclusive jet cross sections*, Phys. Rev. D**57** (1998), 5787.

[37] C.F. Berger, C. Marcantonini, I.W. Stewart, F. J. Tackmann and W. J. Waalewijn, *Higgs production with a central jet veto at NNLL+NNLO*, JHEP**04** (2011) 092, arXiv:1012.448 [hep-ph].

[38] A. Banfi, G. P. Salam and G. Zanderighi, *Phenomenology of event shapes at hadron colliders*, JHEP**06** (2010) 038, arXiv: 1001.4082 [hep-ph].

[39] A. Banfi, G. P. Salam and G. Zanderighi, *Resummed event shapes at hadron-hadron colliders*, JHEP**08** (2004) 062, arXiv: 0407287 [hep-ph].

[40] M. Cacciari, G. P. Salam and G. Soyez, *FastJet user manual*, Eur. Phys. J. C**72** (2012), arXiv: 1111.6097 [hep-ph].

[41] M. Cacciari, G. P. Salam and G. Soyez, *The Anti-k(t) jet clustering algorithm*, JHEP**04** (2008) 063, arXiv: 0802.1189 [hep-ph].

[42] M. Cacciari, G. P. Salam and G. Soyez, *The Catchement Area of Jets*, JHEP**04** (**2008**) p. 005, arXiv: 0802.1188 [hep-ph].

[43] M. Cacciari and G. P. Salam, *Dispelling the $N^3$ myth for the $k_t$ jet-finder*, Phys. Lett. B**641** (2006), p. 57. arXiv: 0512210 [hep-ph].

[44] J. Alwall, R. Frederix, S. Frixione, V. Hirschi, F. Maltoni, O. Mattelaer, H. S. Shao, T. Stelzer, P. Torrielli, and M. Zaro, *The automated computation of tree-level and next-to-leading order differential cross sections, and their matching to parton shower simulations*, JHEP**07** (2014) 079, arXiv: 1405.0301 [hep-ph].

[45] S. Hoeche, F. Krauss, N. Lavesson, L. Lonnblad, M. Mangano, A. Schalicke, and S. Schumann, *Matching parton showers and matrix elements*, in HERA and the LHC: A Workshop on the implications of HERA for LHC physics: Proceedings Part A, pp. 288-289. 2005. arXiv: 0602031 [hep-ph].

[46] P. Skands, S. Carrazza, and J. Rojo, *Tuning PYTHIA 8.1: the Monash 2013 Tune*, European Physical Journal C**74** (2014) 3024, arXiv: 1404.5630 [hep-ph].

[47] R. D. Ball, and al., *Parton distributions with LHC data*, Nucl. Phys. B**867** (2013) 244-289, arXiv: 1207.1303 [hep-ph].

[48] A. Buckley, J. Butterworth, L. Lonnblad, H. Hoeth, J. Monk *et al.*, *Rivet user manual*, arXiv:1003.0694 [hep-ph].

[49] CMS Collaboration, *First measurement of hadronic event shapes in pp collisions at* $\sqrt{s} = 7$ *TeV*, Phys. Lett. B**699** (2011) 48-67, arXiv:1102.0068 [hep-ex].

[50] T. Sjostrand, S. Mrenna, and P. Skands,, *PYTHIA 6.4 Physics and Manual*, JHEP **05** (2006) 026, arXiv: 0603175 [hep-ph].

[51] T. Sjostrand, S. Mrenna, and P. Skands, *A brief introduction to Pythia 8.1*, Compt.Phys.Commun. **178** (2008) 852-867, arXiv:0710.3820 [hep-ph].

[52] T. Sjöstrand and M. van Zijl, *A Multiple Interaction Model for the Event Structure in Hadron Collisions*, Phys. Rev. D**36** (1987), 2019.

[53] B. Andersoon, G. Gustafson, G. Ingelman and T. Sjöstrand, *Parton fragmentation and string dynamics*, Phys. Rep. **97**(1983) 31.

[54] D. Amati and G. Veneziano, *Preconfinement as a Property of Perturbative QCD*, Phys. Lett. B**83** (1979) 87.

[55] P. Skands and D. Wicke, *Non-perturbative QCD effects and the top mass at the Tevatron*, Eur. Phys. J. C**52** (2007) 133.

[56] R. Field. *The Underlying Event in Hard Scattering Processes*, arXiv: 0201192 [hep-ph].

[57] DØ Collaboration, *Measurement of color flow in $t\bar{t}$ events from $p\bar{p}$ collisions at $\sqrt{s} = 1.96$ TeV*, Phys. Rev. **D83** (2011) 092002, arXiv: 1101.0648 [hep-ex].

[58] ATLAS Collaboration, *Measurement of color flow with the jet pull angle in $t\bar{t}$ events using the ATLAS detector at $\sqrt{s} = 8$ TeV*, Physics Letters B (2015) 475-493, arXiv: 1506.05629 [hep-ex]

[59] S. Argyropoulos and T. Sjöstrand, *Effects of color reconnection on $t\bar{t}$ final states at the LHC*, JHEP**1411** (2014) 043.

[60] P. Nason, *A new method for combining NLO QCD with shower Monte Carlo Algorithms*, JHEP**11** (2004) 040.

[61] S. Frixione, P. Nason and C. Oleari, *Matching NLO QCD computations with Parton Shower simulations: the POWHEG method*, JHEP**11** (2007) 70.

[62] S. Alioli, P. Nason, C. Oleari and E. Re, *A general framework for implementing NLO calculations in shower Monte Carlo programs: the POWHEG BOX*, JHEP**06** (2010) 043.

[63] D.J. Lange, *The EvtGen particle decay simulation package*, Nucl. Instrum. Meth. A **462** (2001) 152.

[64] NNPDF Collaboration, *Parton distributions with LHC data*, Nucl. Phys. B **867** (2013) 244, arXiv:hep-ph/1207.1303.

[65] NNPDF Collaboration, *Parton distributions for the LHC Run II*, JHEP **04** (2015) 040, arXiv:1410.8849.

[66] ATLAS Collaboration, *ATLAS Pythia 8 tunes to 7 TeV data*, ATL-PHYS-PUB-2014-021 (2014).

[67] ATLAS Collaboration, *The ATLAS Simulation Infrastructure*, Eur. Phys. J. C **70** (2010) 823, arXiv:1005.4568 [physics.ins-det].

[68] S. Agostinelli *et* al., *GEANT4: A simulation toolkit*, Nucl. Instrum. Meth. A **506** (2003) 250.

[69] ATLAS Collaboration, *Performance of the ATLAS Inner Detector track and vertex reconstruction in the high pile-up LHC environment*, ATLAS-CONF-2012-042 (2012).

[70] ATLAS Collaboration, *The new ATLAS track reconstruction (NEWT)*, J. Phys. Conf. Ser. **119** (2008) 032014.

[71] ATLAS Collaboration, *Reconstruction of primary vertices at the ATLAS experiment in Run I protonproton collisions at the LHC*, Eur. Phys. J. C **77** (2016) 332, arXiv: 1611.10235 [hep-ex].

[72] ATLAS Collaboration, *Muon reconstruction performance of the ATLAS detector in proton-proton collision data at* $\sqrt{s} = 13TeV$, Eur. Phys. J. C **76** (2016) 292, arXiv: 1603.05598 [hep-ex].

[73] ATLAS Collaboration, *Performance of the ATLAS track reconstruction algorithms in dense environments in LHC Run II*, Eur. Phys. J. C **77** (2017) 673, arXiv: 1704.07983 [hep-ex].

[74] ATLAS Collaboration, *Topological cell clustering in the ATLAS calorimeters and its performance in LHC Run I*, Eur. Phys. J. C **77** (2017) 490, arXiv: 1603.02934 [hep-ex].

[75] ATLAS Collaboration, *Jet energy scale measurements and their systematic uncertainties in proton-proton collisions at* $\sqrt{s} = 13$ *TeV with the ATLAS detector*, Phys. Rev. D **96** (2017), arXiv: 1703.09665 [hep-ex].

[76] ATLAS Collaboration, *Expected performance of the ATLAS b-tagging algorithms in Run II*, ATL-PHYS-PUB-2015-022 (2015).

[77] ATLAS Collaboration, *Commissioning of the ATLAS b-tagging algorithms using* $t\bar{t}$ *events in early Run II data*, ATL-PHYS-PUB-2015-039 (2015).

[78] ATLAS Collaboration, *Optimisation of the ATLAS b-tagging performance for the 2016 LHC Run*, ATL-PHYS-PUB-2016-012 (2016).

[79] ATLAS Collaboration, *Performance of algorithms that reconstruct missing transverse momentum in $\sqrt{s} = 8$ TeV proton-proton collisions in the ATLAS detector*, Eur. Phys. J. C **77** (2017), arXiv: 1609.09324 [hep-ex].

[80] S. Argyropoulos and T. Sjöstrand, *Effects of color reconnection on $t\bar{t}$ final states at the LHC*, JHEP**11** (2014) 043, arXiv:1407.6653 [hep-ph].

[81] S. Schmitt, *Data unfolding methods in high energy physics*, EPJ Web Conf. **137**(2017).

[82] F. Wilk, *Synesthesia  The art of seeing QCD color: A measurement of color flow in top-quark pair events*, Thesis submitted to the University of Manchester for the degree of PhD, 2018.